

CHAPTER ONE

Multiscale Modelling of Dense Gas–Particle Flows

**Maike W. Baltussen, Kay A. Buist, Elias A.J.F. Peters,
Johannes A.M. Kuipers¹**

Multiphase Reactors Group, Eindhoven University of Technology, Eindhoven, The Netherlands

¹Corresponding author: e-mail address: J.A.M.Kuipers@tue.nl

Contents

1. Introduction	4
2. DNS	8
2.1 Governing Equations DNS	9
2.2 Numerical Solution Method DNS	11
2.3 Results DNS	13
3. DEM	21
3.1 Governing Equations DEM	22
3.2 Numerical Solution Method DEM	24
3.3 Results DEM	27
4. TFM	30
4.1 Governing Equations TFM	32
4.2 Numerical Solution Method TFM	35
4.3 Results TFM	37
5. Conclusions and Outlook	49
Acknowledgments	50
References	50

Abstract

In large-scale industrial processes involving granulation, coating, and production of base chemicals and polymers dense particulate flows with coupled mass, momentum, and heat transfer are frequently encountered. Both (effective) fluid–particle and (dissipative) particle–particle interactions need to be accounted for because the mutual competition between these phenomena govern the key features of dense gas–particle flows such as regime transitions. These interactions prevail at different length scales and consequently a multiscale approach is adopted to arrive at a quantitative description of these complex flows. In this approach detailed models, taking into account the relevant details of fluid–particle interaction (DNS) and particle–particle interaction (DEM) are used to obtain closure laws to feed two-fluid models (TFMs) which can be used to simulate the flow on a much larger (industrial) scale. In this chapter, we will discuss recent advances in the multiscale simulation of dense gas–fluidized beds. The governing

equations will be presented as well as the key features of the numerical solution method. For each model type, illustrative computational results will be presented. Finally, areas which need substantial further attention will be discussed.

ABBREVIATIONS

CFD	computational fluid dynamics
CFM	continuous forcing method
CPU	central processing unit
CSTR	continuously stirred tank reactor
DFM	direct forcing method
DIA	digital image analysis
DNS	direct numerical simulation
DPM	discrete particle model
DEM	discrete element model
EL	Euler–Lagrange
FOU	first-order upwind
ICGM	incomplete conjugate gradient method
IBM	immersed boundary method
KTGF	kinetic theory of granular flow
LBM	Lattice Boltzmann method
LLDPE	linear low-density polyethylene
MD	molecular dynamics
ODE	ordinary differential equation
PDF	probability density function
PEPT	positron emission particle tracking
PIV	particle image velocimetry
PRS	particle resolved simulation
STA	simultaneous thermal analysis
TFM	two-fluid model
TGA	thermogravimetric analysis
TVD	total variation diminishing
UPW	upwind

NOTATION

$C_{i,f}$	concentration of species i (mole/m ³)
$\langle C_{A,f} \rangle$	flow-average concentration of species A (mole/m ³)
C_d	drag coefficient (–)
C_p	heat capacity (J/(kg K))
C_m	net convective mass flux (mole/(m ³ s))
C_h	net convective heat flux (W/m ³)
d_p	particle diameter (m)
D	mass defect according to the continuity equation (kg/m ³)
$D(\bar{r})$	distribution function (–)
$D_{i,f}$	diffusivity of species i in the fluid (m ² /s)
e_n	normal restitution coefficient (–)

F	dimensionless drag coefficient (–)
g_0	radial distribution function (–)
I_p	particle moment of inertia (kg m^2)
J_g	Jacobian for pressure correction (s^2/m^2)
J_s	Jacobian for voidage correction (kg/m^3)
k_m	fluid–particle mass transfer coefficient (m/s)
m_p	particle mass (kg)
Nu	particle Nusselt number (–)
p, P	pressure (N/m^2)
r	radial coordinate (m)
Pr	Prandtl number (–)
Re_p	particle Reynolds number (–)
T	temperature (K)
$\langle T_f \rangle$	flow-average temperature (K)
t	time (s)
U	superficial gas velocity (m/s)
z	axial coordinate (m)

GREEK LETTERS

α	specific interphase heat transfer coefficient (W/m^3)
α_p	fluid–particle heat transfer coefficient (W/m^2)
β	interphase momentum transfer coefficient ($\text{kg}/(\text{m}^3 \text{ s})$)
Δt	time step (s)
Δp_g	pressure correction (N/m^2)
$\Delta \varepsilon_g$	voidage correction (–)
ΔH_r	heat of reaction (J/mol)
ε	volume fraction (–)
ϕ	angle (–)
Φ	specularity coefficient (–)
$\Phi_{m,f \rightarrow s}$	fluid–particle mass transfer rate (mole/s)
$\Phi_{h,f \rightarrow s}$	fluid–particle heat transfer rate (W)
$\overline{\Phi}_f$	fluid phase heat flux (W/m^2)
γ	dissipation rate of fluctuation kinetic energy of the solid phase ($\text{kg}/(\text{m s}^3)$)
κ	thermal conductivity ($\text{W}/(\text{m K})$)
λ	bulk viscosity ($\text{kg}/(\text{m s})$)
μ	dynamic viscosity ($\text{kg}/(\text{m s})$)
$\bar{\omega}_p$	particle rotational velocity (s^{-1})
ρ	density (kg/m^3)
θ	granular temperature (m^2/s^2)

VECTORS

\overline{A}	momentum density ($\text{kg}/(\text{m}^2 \text{ s})$)
\overline{C}_m	net convective momentum flux (N/m^3)

$\bar{f}_{f \rightarrow p}$	volumetric force exerted by the fluid on the particles (N/m^3)
$\bar{F}_{f \rightarrow s}$	fluid-particle force (N)
\bar{g}	gravitational acceleration (m/s^2)
$\bar{h}_{f \rightarrow p}$	volumetric fluid-particle heat exchange rate (W/m^3)
\bar{n}	unit outward normal ($-$)
\bar{q}_s	pseudo Fourier heat flux (kg/s^3)
\bar{u}	velocity (m/s)
\bar{w}_p	particle translational velocity (m/s)
$\bar{T}_{f \rightarrow s}$	fluid-particle torque ($N\ m$)

TENSORS

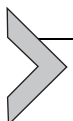
D	rate of deformation tensor (s^{-1})
I	identity tensor ($-$)
τ	viscous stress tensor (N/m^2)

SUBSCRIPTS AND SUPERSCRIPTS

con	convection
e	effective
f	static friction, fluid phase
g	gas phase
mf	minimum fluidization
p	particle phase
s	solid phase
vis	viscous
w	wall

OPERATORS

$\frac{\partial}{\partial t}$	partial time derivative (s^{-1})
∇	gradient operator (m^{-1})
$\nabla \cdot$	divergence operator (m^{-1})



1. INTRODUCTION

Dense gas-particle flows are very often encountered in the process industries involving physical (coating, drying, and granulation) and chemical (synthesis of base chemicals, gasification, and combustion) transformations.

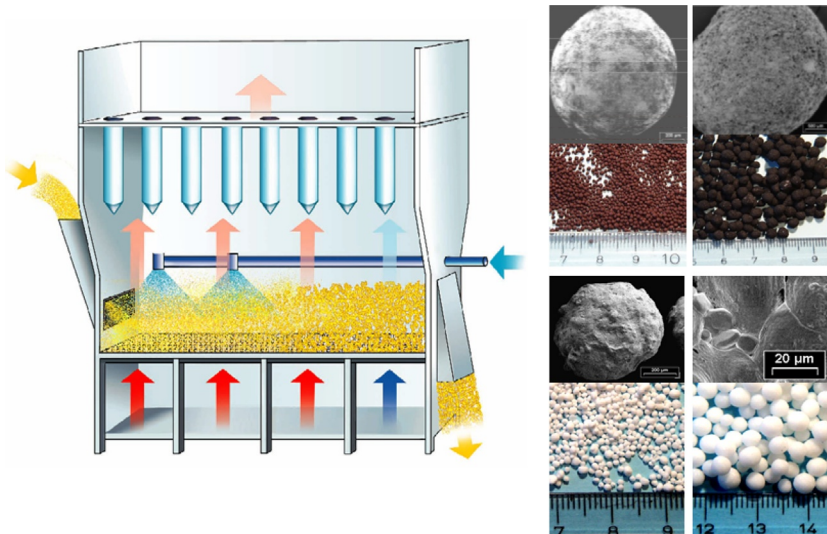


Fig. 1 Schematic representation of a gas-fluidized bed granulator (left) for the production of functional particles (solids inlet and outlet (yellow), hot (red) and cold (dark blue) gas inlet, and liquid binder inlet (light blue)). Examples of functional particles produced in this type of equipment are also shown (right).

In Fig. 1, shown as an example to highlight the complexity of such systems, a schematic representation of a gas-fluidized bed granulator for the production of functional particles is given. This apparatus consists of various sections with solids inlet and outlet, hot and cold gas inlets, and a liquid binder inlet facilitating top spraying of the bed. Binder deposition on the (primary) bed particles causes the growth of the particles to the desired size. Clearly in this unit operation a complex multiscale problem is encountered with poly-disperse dense gas–particle flow accompanied by coupled mass and heat transport. Moreover the introduction of the liquid leads to (partially) wet particles with complicated strongly dissipative particle–particle and particle–wall collisions (Buck et al., 2017; Tang et al., 2017). Such strongly dissipative collisions favor the formation of heterogeneous flow structures with considerable impact on the rate of mass, momentum, and heat exchange and hence on the performance of fluidized beds as multiphase chemical reactors. To further elucidate this aspect, we shown in Fig. 2 simulation results obtained from a hard sphere discrete particle model (DPM) for two-dimensional (2D) riser flow (see Hoomans, 2000).

From Fig. 2, it can be seen that the flow structure for the case with ideal particles produces a much more homogeneous particle distribution in

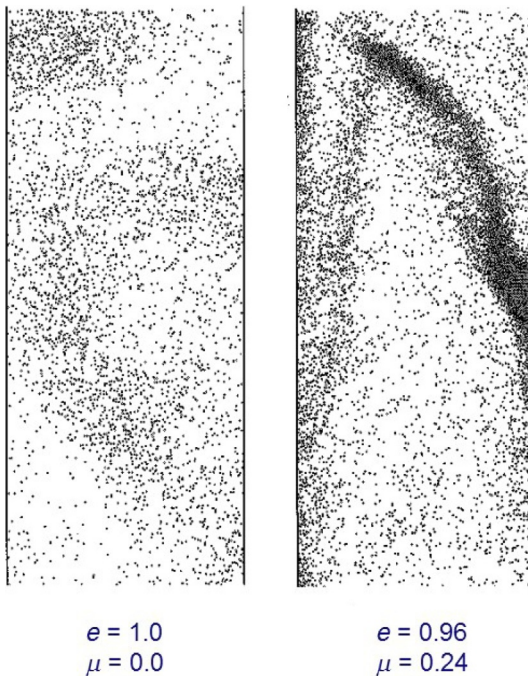


Fig. 2 Simulation results obtained from a hard sphere discrete particle model (DPM) for two-dimensional (2D) riser flow (Hoomans, 2000). Particle size and density: 500 μm and 2660 kg/m^3 , superficial gas velocity: 5.0 m/s, solids flux 25 $\text{kg}/(\text{m}^2 \text{s})$, riser diameter: 0.08 m. *Left:* ideal collisions. *Right:* nonideal collisions. Here e and μ represent, respectively, the normal restitution coefficient and the tangential friction coefficient. Values for the collision parameters for particle–particle and particle–wall collisions are chosen the same.

comparison with the case where the particle collisions are nonideal. For the latter case, despite the fact that the particles are introduced uniformly at the bottom of the riser, due to the dissipative particle–particle and particle–wall collisions heterogeneous flow structures (i.e., so-called strands or clusters) emerge. The riser hydrodynamics is significantly influenced by the presence of strands or clusters and consequently the quality of the gas–solid contact is profoundly influenced and has been subject of extensive experimental and computational studies.

From these two examples, the enormous complexity of dense gas–particle flows is apparent and the associated huge challenge to develop predictive computational tools which can facilitate the optimization and design of gas-fluidized beds. In a broader sense, these tools could aid in improving the performance of plants processing solids that are reported to have been performing below their design expectations during the last decades

([Merrow, 1985](#)). Owing to the continuous increasing computer capacity and rapid developments in computational science detailed simulation of complex multiphase flow phenomena has received a lot of attention during the last few decades.

The hydrodynamic approach to fluidization was started by [Davidson \(1961\)](#) through the analysis of single bubble motion in an infinite bed using two continuity equations and Darcy's law for porous media flow. He assumed irrotational solids flow around the rising gas bubble and his relatively simple model was able to capture the main features of the motion of isolated bubbles in dense gas-fluidized beds and laid the foundation for reactor models of dense gas-fluidized beds involving catalytic conversion ([Kunii and Levenspiel, 1991](#)).

Hydrodynamic modelling of dense gas-fluidized beds was pioneered by Gidaspow and coworkers using the full set of continuum equations (see review paper of [Gidaspow, 1986](#)) and demonstrated the abilities and potential of this approach as a new research and development tool for in depth study of gas-fluidized beds. Their pioneering work triggered the meanwhile massive research on hydrodynamic modelling of gas-fluidized beds and laid the foundation for the development of more advanced hydrodynamic models based on the kinetic theory of granular flow (KTGF) (see [Ding and Gidaspow, 1990](#)).

Their model was derived on basis of the Boltzmann equation for the velocity distribution of particles and can be classified as a generalization of the volume-averaged Navier–Stokes equations proposed by [Anderson and Jackson \(1967\)](#). Contrary to the classical TFM, the KTGF-based model provides closures for the solid phase transport coefficients (such as the shear and bulk viscosity) in terms of the granular temperature which is obtained by solving simultaneously a transport equation for the kinetic energy associated with the fluctuating solids motion. In the classical TFM, the values for the apparent viscosity are obtained from rheological measurements or indirect measurements based on bubble shape ([Kuipers et al., 1992b](#)).

Modern continuum models for dense gas-fluidized beds embedded in commercial CFD packages are typically based on the KTGF. Owing to the very complex phase interactions and the interplay with physical and/or chemical transformations, as evident from the two examples presented in this section, considerable challenges remain to arrive at a thorough fundamental understanding of these flows and development of design tools with significantly improved predictive capabilities. Owing to the fact that a very large variation in time and length scales exists in dense gas–particle flows a multiscale modelling approach has been adopted comprising several CFD models with different degree of sophistication.

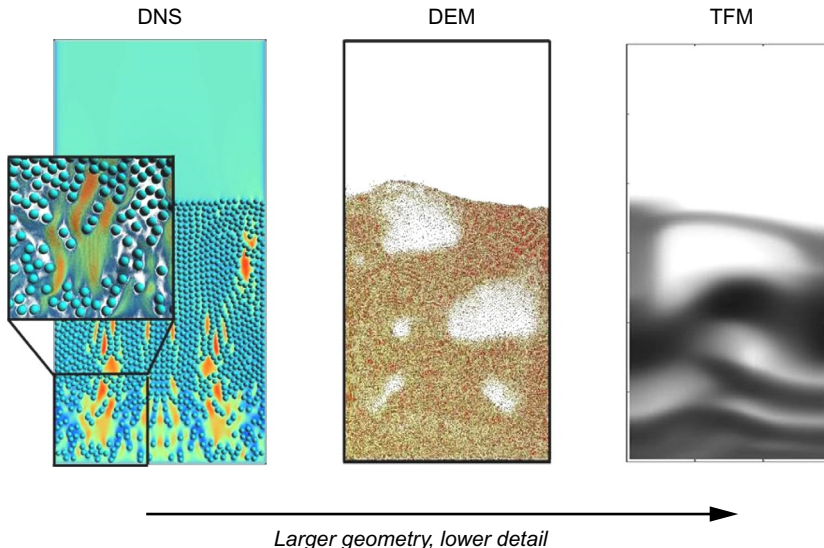


Fig. 3 Multiscale approach for dense gas–particle flows comprising direct numerical simulation (DNS), the discrete element model (DEM), and the two-fluid model (TFM) based on the kinetic theory of granular flow (KTGF). Reproduced with permission from Deen NG, Kuipers JAM: Direct numerical simulation of fluid flow and mass transfer in dense fluid–particle systems, Ind Eng Chem Res 52:11266–11274, 2013.

This multiscale approach for dense gas–particle flows is described in detail by Van der Hoef et al. (2004, 2008) and comprises (see Fig. 3) direct numerical simulation (DNS), the discrete element model (DEM), and the two-fluid model (TFM) or continuum approach based on the KTGF. Subsequently the three levels of modelling comprising the multiscale approach presented in Fig. 3 will be discussed and presented in more detail.

2. DNS

In DNS or particle resolved simulation (PRS), a sufficiently refined computational grid is used to solve the governing equations and captures all relevant details of the flow field at a scale (much) smaller than the size of individual particles. The effective fluid–particle interaction (drag coefficient, heat and mass transfer coefficients) in dense particle swarms is evaluated as a function of the relevant parameters (solids volume fraction, particle Reynolds number, Prandtl (Pr) number, and Schmidt (Sc) number) and subsequently suitably parameterized. The Newtonian equations of motion are solved for the suspended particles while accounting for particle–particle and

particle–wall collisions similar to the approach adopted in DEM. Additional equations for the particles such as species and thermal energy equations can be added with relative ease.

The underlying CFD methods are typically based on either fixed grids or body-conforming grids. Fixed grid methods such as the immersed boundary method (IBM) are preferred in case many moving particles need to be considered because the dynamic remeshing required in methods using body-conforming grids becomes very CPU demanding. Of course as an alternative the Lattice Boltzmann method (LBM) can be used as well. The IBM has gained considerable interest in recent years to handle flows in complex geometries due to the fact that this method is very CPU (and memory) efficient. Roughly two main types of IBM methods can be distinguished: continuous forcing methods (CFM) and direct forcing methods (DFM). In CFM, suitable source terms are added to the transport equations to enforce the boundary condition (for instance the Dirichlet condition) at the boundary of the immersed object, whereas in DFM this boundary condition is enforced at the level of the discretized transport equations. For details the interested reader is referred to excellent reviews by [Peskin \(2002\)](#), [Mittal and Iaccarino \(2005\)](#), and furthermore to [Deen et al. \(2012\)](#) and [Deen and Kuipers \(2013, 2014\)](#) detailing our IBM based on a ghost fluid approach.

2.1 Governing Equations DNS

The system of interest requires the simultaneous solution of the fluid phase and solid (particle) phase equations. For the model presented in this chapter, we make use of the following main assumptions:

- The fluid phase is incompressible and obeys the Newtonian stress closure model.
- All physical properties of the fluid phase and solids phase are constant.
- The solid phase consists of spherical catalyst particles where at the surface of the particles an infinitely fast chemical reaction involving a single chemical species A with associated heat effect takes place.
- Intraparticle temperature gradients are negligible.

2.1.1 Fluid Phase Equations

The transport phenomena in the fluid phase are governed by the conservation equations for mass, momentum, thermal energy, and chemical species, respectively, given by:

$$(\nabla \cdot \bar{u}) = 0 \quad (1)$$

$$\frac{\partial \rho_f \bar{u}}{\partial t} + (\nabla \cdot \rho_f \bar{u} \bar{u}) = -\nabla p + \mu_f \nabla^2 \bar{u} + \rho_f \bar{g} \quad (2)$$

$$\rho_f C_{p,f} \left[\frac{\partial}{\partial t} (T_f) + (\nabla \cdot \bar{u} T_f) \right] = \kappa_f \nabla^2 T_f \quad (3)$$

$$\frac{\partial c_{i,f}}{\partial t} + (\nabla \cdot c_{i,f} \bar{u}) = D_{i,f} \nabla^2 c_{i,f} \quad i = 1, \dots, N \quad (4)$$

In these equations, ρ_f , μ_f , $C_{p,f}$, κ_f represent, respectively, the density, viscosity, heat capacity, and thermal conductivity of the fluid, whereas $D_{i,f}$ represents the diffusivity of species “ i ” in the fluid. These equations are coupled to the particle equations which are given subsequently.

2.1.2 Particle Equations

The translational and rotational motion of the suspended solid particles is governed by the Newtonian equations of motion, respectively, given by:

$$m_p \frac{d\bar{w}_p}{dt} = m_p \bar{g} + \bar{F}_{f \rightarrow s} \quad (5)$$

and

$$I_p \frac{d\bar{\omega}_p}{dt} = \bar{T}_{f \rightarrow s} \quad (6)$$

where m_p and I_p represent, respectively, the mass and the moment of inertia of the particle. The final terms on the right-hand sides in Eqs. (5) and (6) account for the fluid–particle interaction (respectively, drag and torque). The particle temperature is governed by (assuming uniform particle temperature) the following equation:

$$m_p C_{p,p} \frac{dT_p}{dt} = \Phi_{h,f \rightarrow s} + \Phi_{m,f \rightarrow s} (-\Delta H_r) \quad (7)$$

The first term on the right-hand side of Eq. (7) accounts for the heat transfer rate from the fluid to the particle, whereas the second term represents the heat source associated with a mass transfer limited exothermal surface reaction. The drag, torque, and the fluid–particle mass and heat transfer rates are computed once the solution of the fluid phase equations has been completed.

2.2 Numerical Solution Method DNS

The first step involves the time discretization of the momentum equation leading to the following expression:

$$\alpha[\rho_f \bar{u}^{n+1}] = \beta[\rho_f \bar{u}^n] + \gamma[\rho_f \bar{u}^{n-1}] - \Delta t \nabla p^{n+1} - \Delta t \bar{C}_m^n + \Delta t [\mu_f \nabla^2 \bar{u}^{n+1}] + \rho_f \bar{g} \Delta t \quad (8)$$

where n indicates the time index and \bar{C}_m the net convective momentum flux given by:

$$\bar{C}_m = \rho_f (\nabla \cdot \bar{u} \bar{u}) \quad (9)$$

For the discrete representation of the time derivative, we use a second-order three-point backward scheme (with $\alpha = 1.5$, $\beta = 2.0$, and $\gamma = -0.50$) requiring three levels of storage for the velocity components. For the first time step however level ($n - 1$) is not available and consequently in this case: $\alpha = 1.0$, $\beta = 1.0$, and $\gamma = 0.0$ is used. For the solution of Eq. (8), a two-step projection method is used whereas a first step a tentative velocity field \bar{u}^{**} is computed from:

$$\alpha[\rho_f \bar{u}^{**}] = \beta[\rho_f \bar{u}^n] + \gamma[\rho_f \bar{u}^{n-1}] - \Delta t \bar{C}_m^n + \Delta t [\mu_f \nabla^2 \bar{u}^{**}] + \rho_f \bar{g} \Delta t \quad (10)$$

For the Laplace operator standard central second-order finite difference representations are used whereas the convection terms are evaluated with a second-order flux delimited Barton scheme (Centrella and Wilson, 1984). The final ($n + 1$) velocities are obtained from the following equation where the tentative (intermediate) velocity field is corrected to include the effect of the pressure gradient:

$$\bar{u}^{n+1} = \bar{u}^{**} - \frac{\Delta t}{\alpha \rho_f} \nabla p^{n+1} \quad (11)$$

The pressure at the new time level is computed from the Poisson equation which can be obtained by taking the divergence of Eq. (11) and enforcing continuity on the final ($n + 1$) velocity field:

$$\frac{1}{\rho_f} \nabla^2 p^{n+1} = \frac{\alpha}{\Delta t} (\nabla \cdot \bar{u}^{**}) \quad (12)$$

Once the solution of the momentum equations has been achieved the thermal energy equation and the species conservation equation are solved

using the same temporal discretization scheme as applied for the momentum equation:

$$\alpha[\rho_f C_{p,f} T_f^{n+1}] = \beta[\rho_f C_{p,f} T_f^n] + \gamma[\rho_f C_{p,f} T_f^{n-1}] - \Delta t C_h^n + \Delta t [\kappa_f \nabla^2 T_f^{n+1}] \quad (13)$$

$$\alpha c_{A,f}^{n+1} = \beta c_{A,f}^n + \gamma c_{A,f}^{n-1} - \Delta t C_m^n + \Delta t [D_{A,f} \nabla^2 c_{A,f}^{n+1}] \quad (14)$$

where the net convective heat flux C_h^n and the net convective species molar flux C_m^n are given, respectively, by:

$$C_h^n = \rho_f C_{p,f} (\nabla \cdot \bar{u} T_f)^n \quad (15)$$

$$C_m^n = (\nabla \cdot \bar{u} c_{A,f})^n \quad (16)$$

For the spatial discretization of the convection and diffusion terms appearing in the thermal energy and species equations, we have used exactly the same schemes as for the solution of the momentum equations. For the solution of the algebraic equations resulting from the spatial discretization of Eqs. (10), (12), (13), and (14), we use a sparse matrix solver based on the incomplete conjugate gradient method (ICGM).

For the time integration of the solid phase equations (which we solve after the fluid phase equations), we use the trapezoidal rule which offers second-order accuracy and lead to the following equations:

$$\bar{w}_p^{n+1} = \bar{w}_p^n + \bar{g} \Delta t + \frac{\Delta t}{2m_p} [\bar{F}_{f \rightarrow s}^n + \bar{F}_{f \rightarrow s}^{n+1}] \quad (17)$$

$$\bar{\omega}_p^{n+1} = \bar{\omega}_p^n + \frac{\Delta t}{2I_p} [\bar{T}_{f \rightarrow s}^n + \bar{T}_{f \rightarrow s}^{n+1}] \quad (18)$$

$$T_p^{n+1} = T_p^n + \frac{\Delta t}{2m_p C_{p,p}} [\Phi_{h,f \rightarrow s}^n + \Phi_{h,f \rightarrow s}^{n+1} + (\Phi_{m,f \rightarrow s}^n + \Phi_{m,f \rightarrow s}^{n+1})(-\Delta H_r)] \quad (19)$$

As indicated in beginning of [Section 2](#) in immersed boundary techniques several fluid–solid (mass, momentum, and heat) coupling schemes can be adopted. In our technique, we enforce the (Dirichlet) boundary conditions at the level of the discrete form of the field equations with the method described in more detail in [Deen et al. \(2012\)](#) and [Deen and Kuipers \(2013, 2014\)](#). The advantages of this method are its relative simple computer implementation and second-order accuracy. The second feature is beneficial when dealing with many-particle systems because it allows to use a relatively low number of grid points distributed over the particle diameter.

More complex boundary conditions including the treatment of, for instance, conjugate mass, heat transport, and surface reactions can be treated as well (see, respectively, Das et al., 2017 and Lu et al., 2018).

2.3 Results DNS

2.3.1 Flow and Heat Transfer in Stationary Particle Arrays

As an example to demonstrate the capabilities of the DNS approach, in this section we will consider the flow through a stationary random array of hundreds of particles accompanied by mass and heat transfer and exothermic chemical reaction at the surface of the particles (see Table 1 for the data used

Table 1 Data Used for Simulation of Mass Transfer Limited Exothermal Chemical Reaction at the Surface of a Stationary Array of Spheres

Computational grid	$200 \times 200 \times 600 = 24,000,000$	(–)
Grid size	0.0005	m
Time step	0.0001	s
Particle radius	0.0060	m
Initial sphere positions	Random particle configuration (663 spheres) $0.0 < x\text{-position} < 0.100$ $0.0 < y\text{-position} < 0.100$ $0.0 < z\text{-position} < 0.200$ bed voidage $\varepsilon = 0.7001$	
Fluid density	1.0	kg/m^3
Fluid viscosity	2.0×10^{-5}	$\text{kg}/(\text{m s})$
Fluid diffusivity	2.0×10^{-5}	m^2/s
Fluid thermal conductivity	0.025	$\text{W}/(\text{m K})$
Fluid heat capacity	1000.0	$\text{J}/(\text{kg K})$
Fluid inlet temperature	293.0	K
Fluid initial temperature	293.0	K
Particle volumetric heat capacity	1000.0	J/m^3
Particle initial temperature	293.0	K
Reaction heat	−100,000	$\text{J}/(\text{mole})$
Particle Reynolds number	180	(–)

in the simulation). Further details of the model can be found in [Deen et al. \(2012\)](#) and [Deen and Kuipers \(2013, 2014\)](#) as well as extensive verification and validation of the computational methods. The spheres were distributed in a random fashion over the computational domain (excluding the top section with $z > 0.20$ m) using a standard Monte Carlo procedure to produce a predefined voidage of approximately 0.70. For our calculations, we use $d_p/h = 24$, with h the uniform grid spacing. The incorporation of the empty top section was found to be essential to avoid problems due to recirculation over the outflow boundary at the chosen particle Reynolds numbers ($Re_p > 180$). For the simulation, a prescribed uniform velocity and a prescribed pressure were imposed at, respectively, the bottom and top boundaries. For the other boundaries the no-slip condition was imposed. At the bottom wall, the fluid species concentration and the fluid temperature were set at 1.0 mol/m³ and 293.0 K, respectively. At all remaining walls zero concentration and temperature gradients (homogeneous Neumann boundary condition) were imposed.

For the other lateral boundaries the no-slip condition was imposed. At the bottom wall, the fluid species concentration and the fluid temperature were set at 1.0 mol/m³ and 293.0 K, respectively. For the species conservation equation and the thermal energy equation, respectively, zero concentration and temperature gradients (Neumann boundary condition) were imposed.

The thermal behavior of the system is complex and involves (i) transient heating of particles due to the exothermic chemical reaction at the particle surface; (ii) subsequent heat transfer from the heated particles to the fluid flowing through the interstitial void spaces; and (iii) heat transfer from the fluid to downstream particles. This sequence of steps in fact implies that temperature waves propagate through the domain where the heat produced by the exothermic chemical reaction temporarily stored in the particles is swept downstream by the fluid and transferred to relatively cold particles. In [Fig. 4](#), the evolution of the temperature distributions in the system is shown for the vertical central plane (the particles are excluded from the figures) at $Re_p = 180$. From [Fig. 4](#), it can be seen that particles with (nearly) the same axial coordinate experience different heating rates. This is due to substantial differences in the local fluid–particle mass and heat transfer coefficients caused by the existence of (local) preferential pathways for the fluid. From the DNS results detailed information can be obtained such as the (distribution of) the mass and heat transfer coefficients experienced

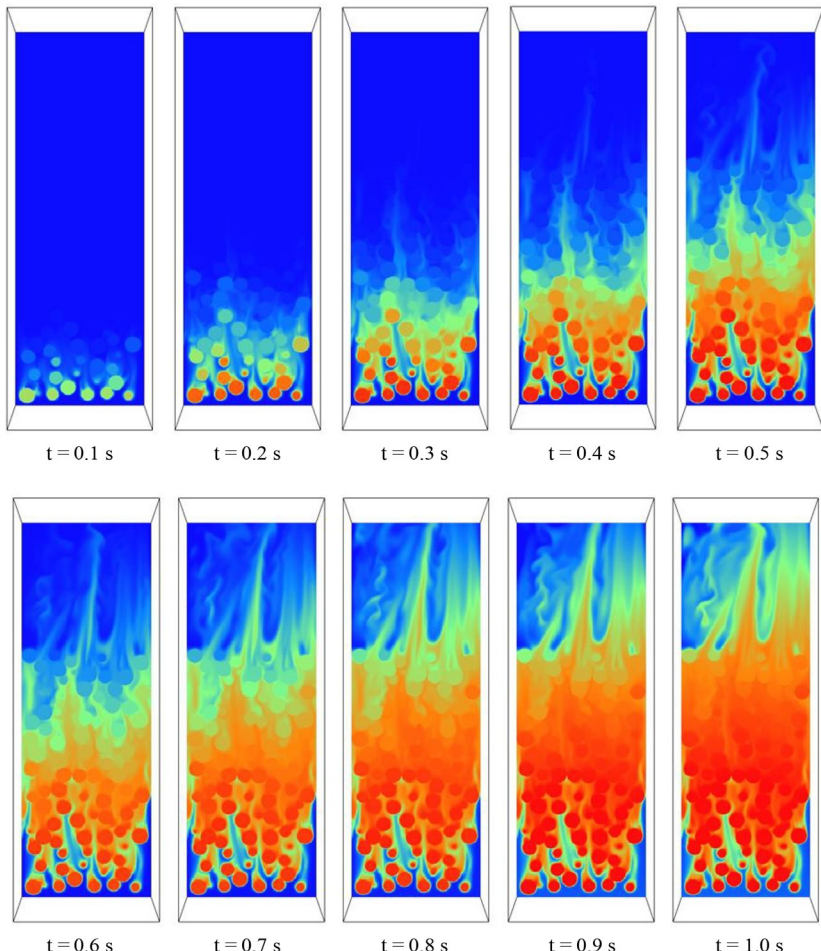


Fig. 4 Evolution of the temperature distribution for $Re_p = 180$ visualized for the central (vertical) yz -plane. The particles are not included in this figure (blue: temperature 293.0 K, red: temperature 393 K). Reproduced with permission from Deen NG, Kuipers JAM: Direct numerical simulation of fluid flow and mass transfer in dense fluid–particle systems, Ind Eng Chem Res 52:11266–11274, 2013.

by individual particles. Here we define the local fluid–particle mass and heat transfer coefficients k_m and α_p by the following equations:

$$k_m = \frac{\Phi_{m,f \rightarrow s}}{4\pi R_p^2 \langle c_{A,f} \rangle} \quad (20)$$

$$\alpha_p = \frac{\Phi_{h,f \rightarrow s}}{4\pi R_p^2 (T_p - \langle T_f \rangle)} \quad (21)$$

where $\Phi_{m,f \rightarrow s}$ and $\Phi_{h,f \rightarrow s}$ represent the mass and heat transfer rates of the surrounding fluid to the particle defined by:

$$\Phi_{m,f \rightarrow s} = - \iint_{S_p} (D_{A,f} \nabla c_{A,f} \cdot \bar{n}) dS \quad (22)$$

$$\Phi_{h,f \rightarrow s} = - \iint_{S_p} (\kappa_f \nabla T_f \cdot \bar{n}) dS \quad (23)$$

Note that for the evaluation of the local driving force in Eqs. (20) and (21) the local (i.e., corresponding to the local z -value) cup-mixing concentration and cup-mixing temperature are used. These quantities are defined as:

$$\langle c_{A,f} \rangle = \frac{\iint_{S_f} u_z(x, y, z) c_{A,f}(x, y, z) dx dy}{\iint_{S_f} u_z(x, y, z) dx dy} \quad (24)$$

$$\langle T_f \rangle = \frac{\iint_{S_f} u_z(x, y, z) T_f(x, y, z) dx dy}{\iint_{S_f} u_z(x, y, z) dx dy} \quad (25)$$

In Table 2, the average mass and heat transport coefficients that are computed using the settings listed in Table 1 are compared (at $t = 1.0$ s) with the corresponding values obtained from the Gunn correlation:

$$Nu_p = \frac{\alpha_p d_p}{\kappa_f} = (7 - 10\epsilon_f + 5\epsilon_f^2) \left(1 + 0.7 (Re_p)^{0.2} (Pr)^{1/3} \right) \\ + (1.33 - 2.40\epsilon_f + 1.20\epsilon_f^2) (Re_p)^{0.7} (Pr)^{1/3} \quad (26)$$

Table 2 Average Values of the Flow-Averaged Mass and Heat Transfer Coefficients Computed From the DNS Data in Comparison With the Mass and Heat Transfer Coefficients Computed From the [Gunn \(1978\)](#) Correlation Using the Data Given in Table 1

Re_p	α_p (W/(m ² K)) DNS	α_p (W/(m ² K)) Gunn (1978)	k_m (m/s) DNS	k_m (m/s) Gunn (1978)
120	25.23	26.87	0.0219	0.0228
180	30.28	31.91	0.0263	0.0272
240	34.33	36.36	0.0298	0.0310

where Re_p and Pr , respectively, represent the particle Reynolds number (based on the superficial velocity U_0) and the Prandtl number:

$$Re_p = \frac{\epsilon_f \rho_f |\bar{u} - \bar{w}_p| d_p}{\mu_f} \quad Pr = \frac{\mu_f C_{p,f}}{\kappa_f} \quad (27)$$

For the evaluation of the fluid–particle heat transfer coefficients particles which have not yet attained their final temperatures are excluded. As can be seen from this table, the agreement between the DNS data and the values obtained from the Gunn correlation is very good.

In Fig. 5, a comparison is presented between the DNS data and results obtained from a 1D heterogeneous model which uses the empirical correlation of Gunn (1978) to evaluate the average value of the mass and heat transfer coefficients.

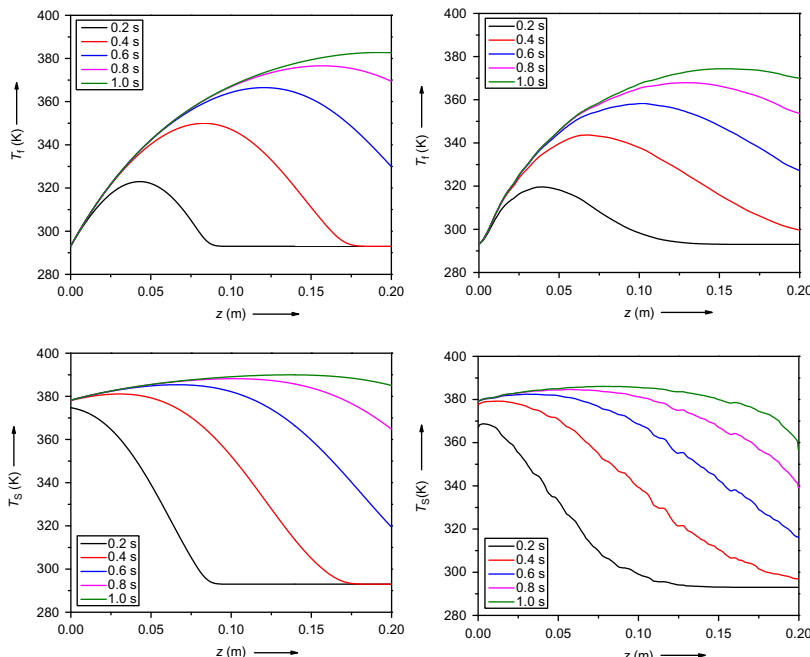


Fig. 5 Vertical profiles of the flow-averaged fluid temperature (top) and the laterally averaged solid (bottom) temperature obtained from a simple one-dimensional (1D) heterogeneous model (left) and DNS (right) at $Re_p = 180$. Reproduced with permission from Deen NG, Kuipers JAM: Direct numerical simulation of fluid flow accompanied by coupled mass and heat transfer in dense fluid–particle systems, Chem Eng Sci 116:645–656, 2014.

The overall features of the transient temperature profiles agree very well but small differences can be observed. First of all, both the maximum temperature and the temperature gradient beyond the maximum obtained from our DNS are lower compared to the results from the 1D heterogeneous model based on plug flow. This difference is caused by the nonuniform velocity profile due to the presence of the particles. Effectively this introduces (minor) axial dispersion of heat and consequently a lower maximum temperature and axial gradient of the temperature.

2.3.2 Fluidization of Spheres in a Pseudo 2D Bed

As a second example, the fluidization of 1296 particles (see [Table 3](#) for the data used in the simulation) will be presented where initially the particles are at rest and distributed over the bottom half of the domain in a lattice with uniform voidage of 0.65. In this case the bed thickness in the depth direction slightly exceeds the particle diameter. The height of the particle free zone is the same as the initial bed height, allowing for expansion of the particle suspension. No-slip boundaries were taken at the walls confining the bed in all the lateral directions whereas a prescribed pressure boundary was taken at the

Table 3 Data Used for the Pseudo 2D Fluidized Bed of Spheres

Computational grid	$400 \times 12 \times 800 = 3,840,000$	(–)
Grid size	0.0005	m
Time step	0.0002	s
Particle radius	0.0025	m
Initial sphere positions	Uniform lattice of $(36 \times 36) = 1296$ Spheres in bottom half of the domain	(–)
Fluid density	1216	kg/m^3
Fluid viscosity	0.100	$\text{kg}/(\text{m s})$
Fluid thermal conductivity	1.0	$\text{W}/(\text{m K})$
Fluid heat capacity	10	$\text{J}/(\text{kg K})$
Superficial liquid velocity	0.08	m/s
Solid density	8000	kg/m^3
Collision parameters e_n, e_t, μ_t	0.90, 0.30, 0.10	(–)

top of the domain. The minimum fluidization velocity for the fluid–particle combination was estimated from the Ergun equation as 1.17 cm/s whereas the terminal velocity of the particle amounted 39.6 cm/s. For the simulation of this thin pseudo 2D fluidized bed, the superficial velocity was set at 8 cm/s.

In Fig. 6, the evolution of the bed particle configuration is shown as a function of time. It can be seen that initially the bed expands uniformly, however near the left and right walls of the bed (due to the no-slip condition) the particle configuration is disturbed producing eventually small cavities which travel near the walls in the vertical direction. In the central part of the bed also disturbances in the particle configuration develop and several cavities start to form and propagate in the vertical direction leading to breakage of the symmetry and consequently a “chaotic” movement and mixing of the particle bed results. Because the superficial velocity u_0 is well above, the minimum fluidization velocity significant expansion of the particle bed occurs. Once the bed expansion is stable the total force exerted by the fluid on particle bed in the vertical direction equals the total weight of the particles (difference less than 1%) however, this balancing of forces does not hold at the level of individual particles. Fig. 7 shows the velocity field of the fluidizing agent in the central plane for a small subdomain of the bed at $t = 2.0$ s revealing a highly nonuniform flow field. The detailed information obtained from this type of simulation is very useful to develop and assess the (drag and heat transfer) closures adopted in models which do not resolve all the details of the flow of the fluidizing agent. The widely used CFD–DEM is a well-known example where typically the computational cells are much larger than the size of an individual particle (Van der Hoef et al., 2008) necessitating specification of closures for the fluid–particle interactions. The average fluid–particle heat transfer coefficient equals 789.0 W/(m² K).

From the bed expansion in the bottom zone of the fluidized bed a (nearly constant) average voidage of 0.80 can be calculated which corresponds to an average fluid–particle heat transfer coefficient of 970.0 W/(m² K) according to the empirical correlation proposed by Gunn (1978).

Besides validating existing closure relations the DNS approach have also been used to estimate closure relation for fluid–particle drag (Das et al., 2016; Mehrabadi et al., 2016; Tang et al., 2015) and fluid–solid heat transfer (Das et al., 2016; Deen et al., 2014). These improved closure relations can next be used in coarser models such as DEM and TFM.

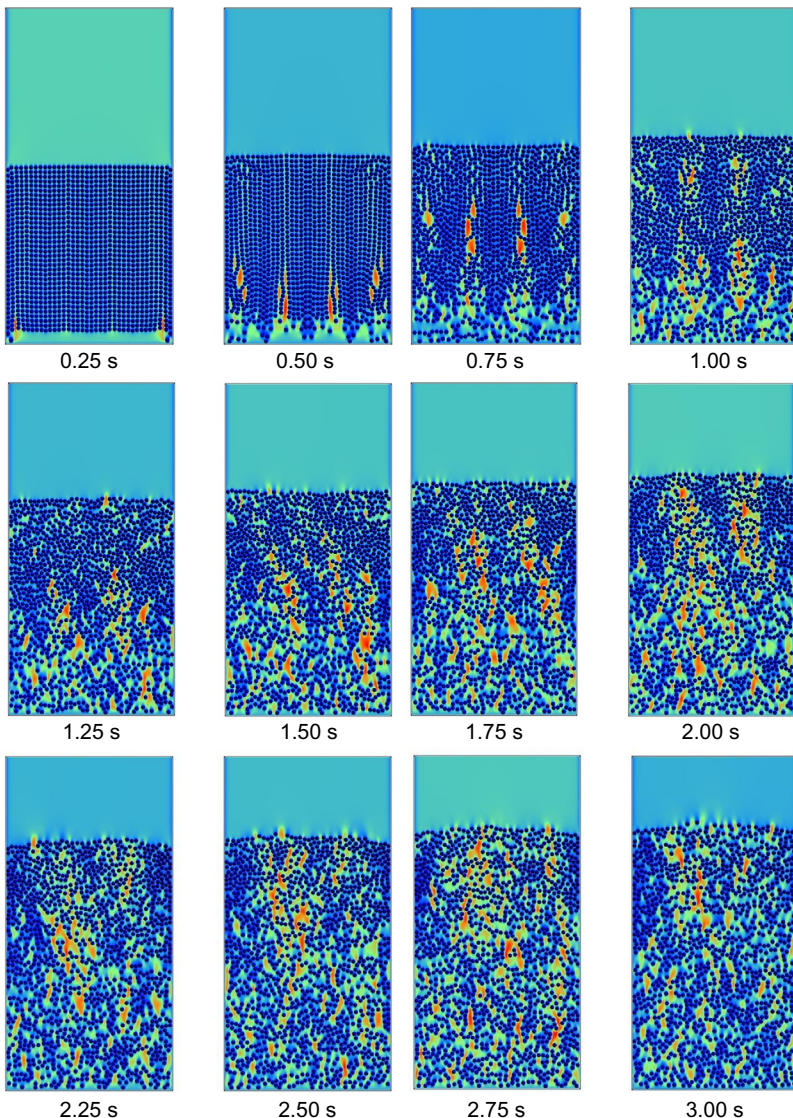


Fig. 6 Evolution of bed structure as a function of time for fluidization of 1296 spheres at superficial velocity of 8 cm/s. Incipient fluidization velocity 1.17 cm/s; terminal velocity 39.6 cm/s. Reproduced with permission from Deen NG, Kriebitzsch SHL, van der Hoef MA, Kuipers JAM: Direct numerical simulation of flow and heat transfer in dense fluid-particle systems, Chem Eng Sci 81:329–344, 2012.

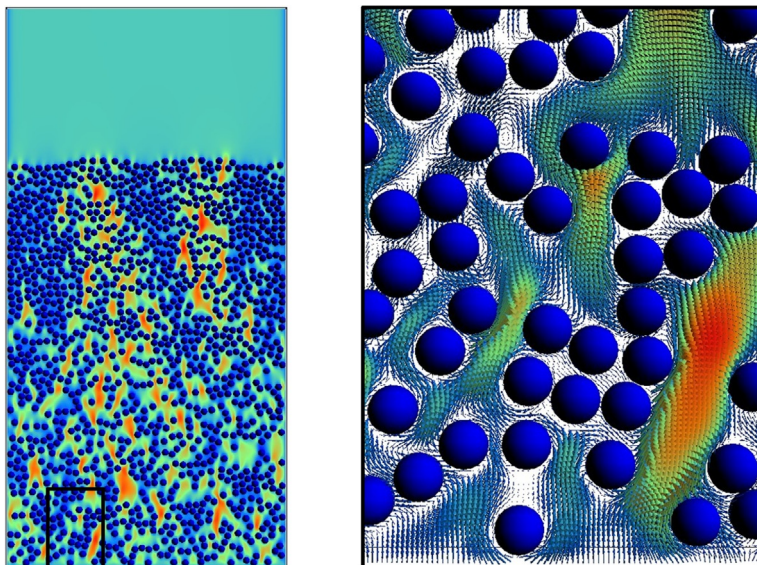


Fig. 7 Particle configuration (left) and velocity map (right) at the central plane for a small subdomain of the bed at $t = 2.00$ s. Incipient fluidization velocity 1.17 cm/s; terminal velocity 39.6 cm/s. Reproduced with permission from Deen NG, Kriebitzsch SHL, van der Hoef MA, Kuipers JAM: Direct numerical simulation of flow and heat transfer in dense fluid-particle systems, Chem Eng Sci 81:329–344, 2012.



3. DEM

In the DEM, the volume-averaged Navier–Stokes equations are solved for the continuous phase whereas the Newtonian equations of motion are solved for each particle while accounting for particle–particle and particle–wall collisions. This type of model can be classified as an unresolved Euler–Lagrange (EL) type of model since typically (unlike the DNS or PRS approach) the computational grid is (much) larger than the size of individual particles and consequently closures for fluid–particle interaction need to be specified either on basis of empirical data or parameterization of DNS data. Both the hard sphere and soft sphere approach have been successfully used to simulate dense gas–fluidized beds.

The hard sphere model assumes binary quasi-instantaneous dissipative collisions and consequently this model is not suited to study granular flow with static regions where multiple particle–particle contacts prevail. For such systems, the soft sphere model is a better choice because it can efficiently handle multiple particle–particle interactions where the pair-wise

interactions are described on basis of a mechanical model comprising a spring, a friction slider, and a dashpot. The SIMPLE algorithm ([Patankar and Spalding, 1972](#)) is used to solve the conservation equations for the continuous phase while the equations of motion for the particulate phase are solved with standard ODE solvers. Efficient algorithms from the field of molecular dynamics (MD) are used for the efficient processing of the large number of (dissipative) collisions. DEM has received a lot of attention in recent years to study complex particulate flows, for further details we refer to the review by [Deen et al. \(2007\)](#).

3.1 Governing Equations DEM

The system of interest requires the simultaneous solution of the gas phase and solid (particle) phase equations. For the model presented in this chapter, we make use of the following main assumptions:

- The fluid phase (gas) is compressible and obeys the ideal gas law.
- The thermophysical properties of both phases are constant.
- The solid phase consists of spherical catalyst particles.
- Intraparticle temperature gradients are negligible.

3.1.1 Fluid Phase Equations

The governing conservation equations for dense fluid–solid flows are given by the following expressions:

$$\frac{\partial}{\partial t}(\varepsilon_f \rho_f) + (\nabla \cdot \varepsilon_f \rho_f \bar{u}) = 0 \quad (28)$$

$$\frac{\partial}{\partial t}(\varepsilon_f \rho_f \bar{u}) + (\nabla \cdot \varepsilon_f \rho_f \bar{u} \bar{u}) = -\varepsilon_f \nabla p - (\nabla \cdot \varepsilon_f \tau_f) - \bar{f}_{f \rightarrow p} + \varepsilon_f \rho_f \bar{g} \quad (29)$$

$$\rho_f C_{p,f} \left[\frac{\partial}{\partial t}(\varepsilon_f T_f) + (\nabla \cdot \varepsilon_f \bar{u} T_f) \right] = -(\nabla \cdot \bar{\Phi}_f) - h_{f \rightarrow p} \quad (30)$$

For the fluid phase stress tensor the general Newtonian form is assumed, given by ([Bird et al., 1960](#)):

$$\tau_f = -\left(\lambda_f - \frac{2}{3}\mu_f\right)(\nabla \cdot \bar{u})I - \mu_f [(\nabla \bar{u}) + (\nabla \bar{u})^T] \quad (31)$$

where μ_f and λ_f are the shear and bulk viscosity of the fluid. For the heat flux $\bar{\Phi}_f$ Fourier's law is assumed:

$$\bar{\Phi}_f = -\kappa_{e,f} \nabla T_f \quad (32)$$

where $\kappa_{e,f}$ represents the effective thermal conductivity of the fluid for which we use the following expression:

$$\kappa_{e,f} = \left(1 - \sqrt{(1 - \varepsilon_f)}\right) \kappa_f \quad (33)$$

where κ_f represents the thermal conductivity of the fluid. The source terms $\bar{f}_{f \rightarrow p}$ and $h_{f \rightarrow p}$ account, respectively, for the two-way coupling of momentum and heat which are obtained from the Lagrangian part of the model which will be discussed later.

3.1.2 Particle phase equations

The motion of the suspended solid particles is given by Newton's second law given by the following expression which accounts for the action of gravity, far-field pressure, and drag.

$$\frac{d}{dt}(m_p \bar{w}_p) = \bar{F}_g + \bar{F}_p + \bar{F}_d = m_p \bar{g} - V_p \nabla p + \frac{V_p \beta_p}{(1 - \varepsilon_f)} (\bar{u} - \bar{w}_p) \quad (34)$$

Since the size of the particles typically is (much) smaller than the size of the computational grid required for capturing the bubble dynamics, a closure equation is required for the effective drag (friction) acting on the particles. Following [Hoomans et al. \(1996\)](#) the friction between the continuous liquid phase and the suspended solid particles is given by the Ergun equation in the dense regime ($\varepsilon_f < 0.8$) and the [Wen and Yu \(1966\)](#) equation in the dilute regime ($\varepsilon_f > 0.8$), respectively, given by

$$(\varepsilon_f < 0.8) \beta_p = 150 \frac{(1 - \varepsilon_f)^2}{\varepsilon_f} \frac{\mu_f}{(d_p)^2} + 1.75(1 - \varepsilon_f) \frac{\rho_f}{d_p} |\bar{u} - \bar{w}_p| \quad (35)$$

and

$$(\varepsilon_f > 0.8) \beta_p = \frac{3}{4} C_d \frac{\varepsilon_f (1 - \varepsilon_f)}{d_p} \rho_f |\bar{u} - \bar{w}_p| (\varepsilon_f)^{-2.65} \quad (36)$$

with the single particle drag coefficient for spheres:

$$C_d = \begin{cases} \frac{24}{Re_p} (1 + 0.15 Re_p^{0.687}) & Re_p < 1000 \\ 0.44 & Re_p > 1000 \end{cases} \quad (37)$$

Alternatively drag closure equations obtained from LB models can be used for the effective drag closure ([Van der Hoef et al., 2008, 2004](#)).

For the (possible) nonideal particle–particle and particle–wall collisions, we use a three-parameter model accounting for normal and tangential restitution and friction. The thermal energy equation for an individual particle is given by:

$$m_p C_{p,p} \frac{dT_p}{dt} = -4\pi R_p^2 \alpha_p (T_p - T_f) \quad (38)$$

where $C_{p,p}$ represents the particle heat capacity and α_p is the fluid–particle heat transfer coefficient given by the empirical equation proposed by Gunn (Eq. 26).

3.2 Numerical Solution Method DEM

First we perform the time discretization of the momentum equation to obtain the following expression:

$$(\epsilon_f \rho_f \bar{u})^{n+1} = \bar{S}_m^n - \Delta t \left[(\epsilon_f \nabla p)^{n+1} + \left(\bar{f}_{f \rightarrow p} \right)^{n+1} \right] \quad (39)$$

where n indicates the time index whereas the explicit terms have been collected in \bar{S}_m^n given by:

$$\bar{S}_m^n = (\epsilon_f \rho_f \bar{u})^n - \Delta t [(\nabla \cdot \epsilon_f \rho_f \bar{u} \bar{u})^n + (\nabla \cdot \epsilon_f \tau_f)^n + (\epsilon_f \rho_f)^n \bar{g}] \quad (40)$$

The viscous terms are treated with standard central second-order finite difference representations whereas the convective terms are computed with a second-order flux delimited Barton scheme (Centrella and Wilson (1984)). A key element in the solution of the momentum equations and the thermal energy equation is the linear implicit treatment of the source terms $\bar{f}_{f \rightarrow p}$ and $h_{f \rightarrow p}$ which account for the two-way coupling caused by the presence of the particles. These terms are now written in, respectively, a part which is independent of the fluid velocity and fluid temperature and a part which, respectively, is proportional to the fluid velocity and the fluid temperature:

$$\bar{f}_{f \rightarrow p}^{n+1} = \bar{\alpha}_{f \rightarrow p}^n(\bar{r}) + \beta_{f \rightarrow p}^n(\bar{r}) \bar{u}(\bar{r})^{n+1} = \frac{1}{V_{cell}} \sum_{p=1}^{p=np} \bar{F}_d(\bar{r}_p) D(\bar{r} - \bar{r}_p) \quad (41)$$

$$h_{f \rightarrow p}^{n+1} = \phi_{f \rightarrow p}^n(\bar{r}) + \varphi_{f \rightarrow p}^n(\bar{r}) T_f(\bar{r})^{n+1} = \frac{1}{V_{cell}} \sum_{p=1}^{p=np} \Phi_h(\bar{r}_p) D(\bar{r} - \bar{r}_p) \quad (42)$$

where $\bar{\alpha}_{f \rightarrow p}^n$, $\beta_{f \rightarrow p}^n$, $\phi_{f \rightarrow p}^n$, and $\varphi_{f \rightarrow p}^n$ are obtained from the Lagrangian part of the model for the particles described hereafter. In Eqs. (41) and (42), the

summation term accounts for the contributions of all particles p which have their center of mass (given by their position vectors \bar{r}_p) within a certain computational cell with volume $V_{\text{cell}} = \Delta x \Delta y \Delta z$. In these expressions, $D(\bar{r})$ represents a distribution function which is decomposed in separate spatial contributions according to the following expression:

$$D(\bar{r}) = D(x, y, z) = D_x(x)D_y(y)D_z(z) \quad (43)$$

For the distribution function $D(\bar{r})$, we typically use volume weighing whereas for the evaluation of the source terms in the momentum equation, care should be taken to account for the staggered computational grid. The sum of the interphase forces is obtained from the Lagrangian part of the model. This particular (linear implicit) treatment of the source terms greatly enhances the numerical stability of the model, especially at high particle volume fraction. Combination of Eqs. (39) and (41) leads to the following expression for the momentum density at the advanced time level:

$$(\varepsilon_f \rho_f \bar{u})^{n+1} = \bar{S}_m^n - \Delta t \left[(\varepsilon_f^{n+1} \nabla p^{n+1}) + \bar{\alpha}_{f \rightarrow p}^n + \beta_{f \rightarrow p}^n \bar{u}^{n+1} \right] \quad (44)$$

or after collecting terms:

$$\left[(\varepsilon_f \rho_f)^{n+1} + \Delta t \beta_{f \rightarrow p}^n \right] \bar{u}^{n+1} = \bar{S}_m^n - \Delta t \left[(\varepsilon_f^{n+1} \nabla p^{n+1}) + \bar{\alpha}_{f \rightarrow p}^n \right] \quad (45)$$

Discretization of the time derivative in the continuity equation leads to the following expression which defines the mass residual D_f^{n+1} :

$$(\varepsilon_f \rho_f)^{n+1} - (\varepsilon_f \rho_f)^n + \Delta t [\nabla \cdot (\varepsilon_f \rho_f \bar{u})^{n+1}] = D_f^{n+1} \quad (46)$$

This mass residual for a certain computational cell (i, j, k) is considered to depend on the pressure in the same computational cell and the pressures of the six surrounding computational cells:

$$\begin{aligned} (D_f)_{i,j,k}^{n+1} &= (D_f)_{i,j,k}^{n+1} \left(p_{i-1,j,k}^{n+1}, p_{i+1,j,k}^{n+1}, p_{i,j-1,k}^{n+1}, p_{i,j+1,k}^{n+1}, p_{i,j,k-1}^{n+1}, p_{i,j,k+1}^{n+1}, p_{i,j,k}^{n+1} \right) \\ &\equiv 0 \end{aligned} \quad (47)$$

which after linearization leads to the following pressure correction equation in vector notation:

$$J \delta \bar{p}^{n+1} = -\bar{D}_f^* \quad (48)$$

where J represents the assembled Jacobi matrix, $\delta\bar{p}^{n+1}$ the vector of (unknown) pressure corrections, and \bar{D}_f^* the vector of known mass residuals computed from the most recently available hydrodynamic field variables. The elements of J can be computed analytically from the definition equation for the mass residual (using central finite difference approximations for the convection terms) and the momentum equation. The resulting (heptadiagonal) sparse matrix equation is again solved with a very efficient ICGM. For each time step only a few (3–4) implicit iterations are required to attain convergence. Following the solution of the continuity and momentum equations, the thermal energy equation of the fluid is solved.

$$\rho_f C_{p,f} (\epsilon_f T_f)^{n+1} = S_h^n + \Delta t \left[(\nabla \cdot \kappa_{f,e} \nabla T_f)^{n+1} - (h_{f \rightarrow p})^{n+1} \right] \quad (49)$$

where n indicates the time index whereas S_h^n represents the explicit term given by:

$$S_h^n = \rho_f C_{p,f} (\epsilon_f T_f)^n - \Delta t \rho_f C_{p,f} (\nabla \cdot \epsilon_f T_f \bar{u})^n \quad (50)$$

Combination of Eqs. (42) and (49) leads to the following expression for the thermal energy equation:

$$\left[\rho_f C_{p,f} \epsilon_f^{n+1} + \Delta t \varphi_{f \rightarrow p}^n \right] T_f^{n+1} = S_h^n + \Delta t \left[(\nabla \cdot \kappa_{e,f} \nabla T_f)^{n+1} - \phi_{f \rightarrow p}^n \right] \quad (51)$$

For the spatial discretization of the convection and conduction terms in, respectively, (50) and (51) exactly the same schemes are used as for the solution of the momentum equations.

The source terms appearing in the Newtonian equations of motion are treated as known (explicit) terms and therefore the integration of these equations can be conducted in principle with any integration technique for ordinary differential equations. For the simulations reported in this chapter, we have used a simple first-order explicit scheme producing translational and rotational particle velocities at the new time level. Once the particle velocities are obtained a collision model (either the hard sphere or soft sphere model) is invoked to account for the particle–particle and particle–wall collisions. The closure of this collision model involves three micro-mechanical parameters: the coefficients for normal and tangential restitution and the tangential friction coefficient, which in principle can be obtained from impact experiments (see Deen et al., 2007). The particle phase thermal energy equation is solved via a first-order linear implicit scheme to obtain the particle temperature at the new time level.

3.3 Results DEM

3.3.1 Gas-Fluidized Beds With Heat Production

Relatively few studies have been reported on the (simultaneous) mass and heat transfer in dense fluid–particle systems. In this section, we will study a gas–fluidized bed with heat production in the particulate phase. This type of system is very often encountered in large-scale processes using dense gas–fluidized beds such as combustion, gasification, partial oxidation of hydrocarbons, and gas phase polymerization for the production of poly–olefines. In the latter process, the monomer (ethylene or propylene) is contacted with a prepolymerized particles containing metallocene type of catalysts leading to very rapid growth of the particles with liberation of a large amount of heat due to the strongly exothermic polymerization reactions.

To avoid the full complexity of catalytic olefin polymerization in the gas phase [Li et al. \(2017\)](#) used CO₂ adsorption on Zeolite 13X particles (1.8–2.0 mm, Geldart D type) as a model system to mimic the heat effect due to the exothermic polymerization reaction. All key aspects of this process (kinetics, equilibrium, and heat effect) were studied separately using thermogravimetric analysis (TGA) and simultaneous thermal analysis (STA). A combined infrared/visual camera technique generated detailed data on the hydrodynamic and thermal behavior of a pseudo 2D bed equipped with a sapphire front glass to minimize the absorption of the emitted thermal radiation. They also compared the evolution of the spatial distribution of the measured particle temperature with CFD–DEM simulation results.

In [Fig. 8](#), we show the comparison of the particulate phase temperature obtained from the experiment (top) with the results obtained from CFD–DEM simulations. From this figure, we can see that the temperature of the particles rises rapidly due to the heat production associated with the CO₂ adsorption. Gradually the adsorption equilibrium is obtained and due to the vanishing heat production and concurrent heat losses to the environment the bed gradually cools down. As evident from [Fig. 6](#), the bed temperature is not uniform due to the fact that (among others) the fluid–particle heat transfer coefficient is a distributed property as shown by [Deen et al. \(2012\)](#) on basis of detailed DNS simulations for dense random arrays of particles. This is due to the fact that (even) in random dense arrays there exist locally preferred pathways of the fluid leading to locally different flow conditions and hence heat transfer rates.

For the CFD–DEM simulations, the [Gunn \(1978\)](#) correlation was used to evaluate the fluid–particle heat transfer coefficient. [Deen and Kuipers \(2014\)](#) showed that the fluid–particle mass and heat transfer coefficients

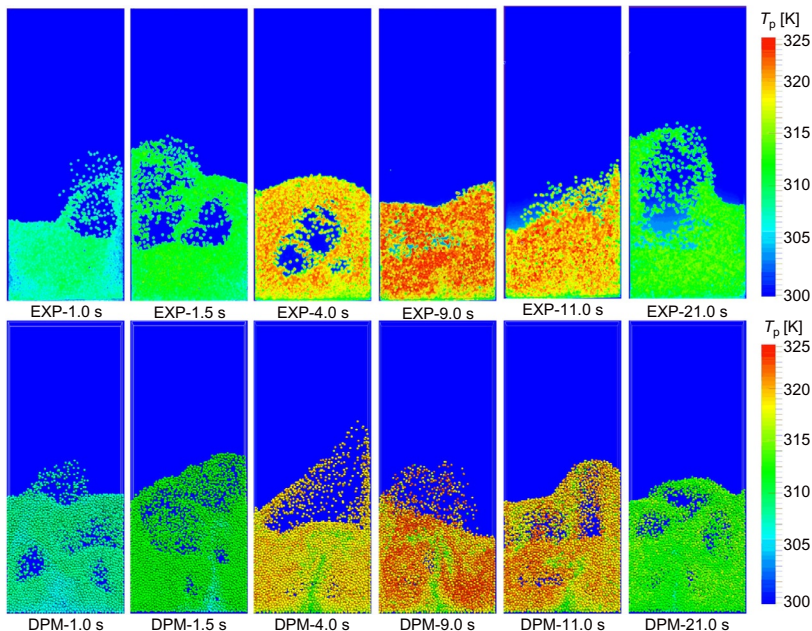


Fig. 8 Comparison of computed evolution of the particulate phase temperature obtained from experiment (top) using infrared (IR) imaging and CFD-DEM (DPM) simulation (bottom). Heat liberation is caused by the CO_2 adsorption on Zeolite 13X particles (1.8–2.0 mm diameter, Geldart D particles). Reproduced with permission from Li Z, Janssen TCE, Buist KA, Deen NG, van Sint Annaland M, Kuipers JAM: Experimental and simulation study of heat transfer in fluidized beds with heat production, Chem Eng J 317:242–257, 2017.

for dense random arrays of particles obtained from DNS simulations agree very well with values obtained from the Gunn correlation. In Fig. 9, the distribution of the particle temperature obtained from the CFD-DEM simulations is compared with the experimental data in terms of the PDF and reveals a very good quantitative agreement between simulation and experiment.

3.3.2 Hydrodynamics of a Pseudo 2D Riser

Riser flows have been studied extensively by using both experimental and computational approaches. Carlos Varas et al. (2017a, 2017b) studied the hydrodynamics of a pseudo 2D riser using a combined digital image analysis (DIA) and particle image velocimetry (PIV). The advantage of the pseudo 2D geometry used by Carlos Varas et al. (2017a, 2017b) is given by the fact that direct visual observation of the heterogeneous flow structures

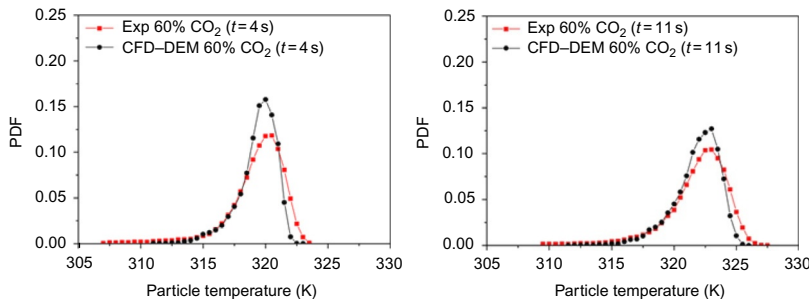


Fig. 9 Comparison of particulate phase temperature PDF obtained from experiment (red) using infrared and CFD-DEM simulation (black). Heat liberation is caused by the CO_2 adsorption on Zeolite 13X particles (1.8–2.0 mm diameter, Geldart D particles). Reproduced with permission from Li Z, Janssen TCE, Buist KA, Deen NG, van Sint Annaland M, Kuipers JAM: Experimental and simulation study of heat transfer in fluidized beds with heat production, Chem Eng J 317:242–257, 2017.

(clusters or strands) is possible enabling detailed characterization and quantification using advanced DIA techniques (see [Carlos Varas et al., 2016](#)). Moreover, since the distance between the front and back plates is rather small, the flow is laminar and consequently uncertainties due to turbulence modelling can be circumvented. In [Fig. 10](#), their experimental setup is shown revealing the presence of heterogeneous flow structures (cluster or strands) descending along the side walls of the riser. They also performed extensive and detailed CFD-DEM simulations and found that the main characteristics of the experimentally observed riser flow could be retrieved from these simulations.

In [Fig. 11](#), both experimental and simulated lateral profiles of the time-averaged solids volume fraction at several heights in the riser are presented from this figure, it can be seen that at relatively low superficial gas velocities a clear lateral segregation occurs which diminishes at higher velocities. The agreement between the experimental and CFD-DEM simulation results is reasonable.

[Carlos Varas et al. \(2017b\)](#) also studied the impact of particle clustering on the gas–solid contact efficiency using detailed CFD-DEM simulations. From their study, it became clear that the gas phase partially circumvents descending dense particle clusters leading to lower gas–solid contact efficiencies. This by-passing induced by heterogeneous flow structures generally leads to lower performance of riser flow reactors as encountered in catalytic cracking processes.

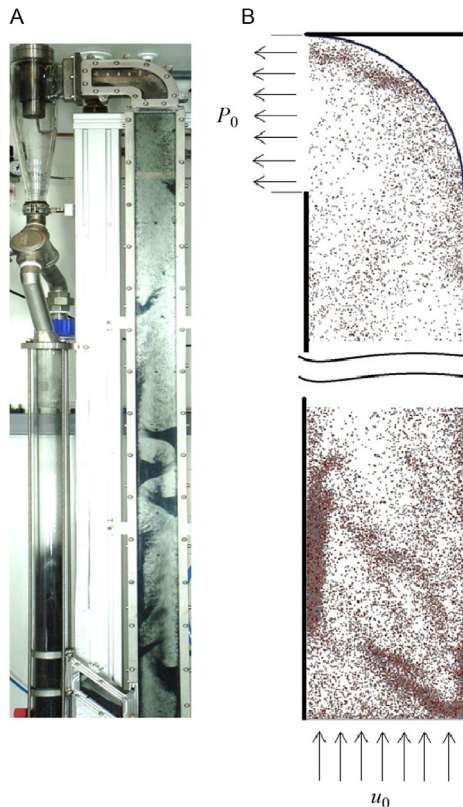
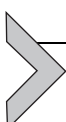


Fig. 10 Pseudo 2D riser (A) showing heterogeneous flow structures descending along the side walls of the riser. In addition, a snapshot (B) of a CFD–DEM simulation is included showing as well-heterogeneous flow structures. *Reproduced with permission from Carlos Varas AE, Peters EAJF, Kuipers JAM: CFD–DEM simulations and experimental validation of clustering phenomena and riser hydrodynamics, Chem Eng Sci 169:246–258, 2017a.*



4. TFM

The TFM is based on the concept of interpenetrating continuous media and employs separate conservation equations for mass, momentum, and heat for each phase. As in the DEM the size of individual particles is much smaller than the size of the computational grid and consequently again closures for fluid–particle interaction need to be defined. Moreover closures for particle–particle interaction are required which in modern continuum models are based on the KTGF. The particle collision models employed in the TFM are typically accounting only for normal restitution. The extension of these

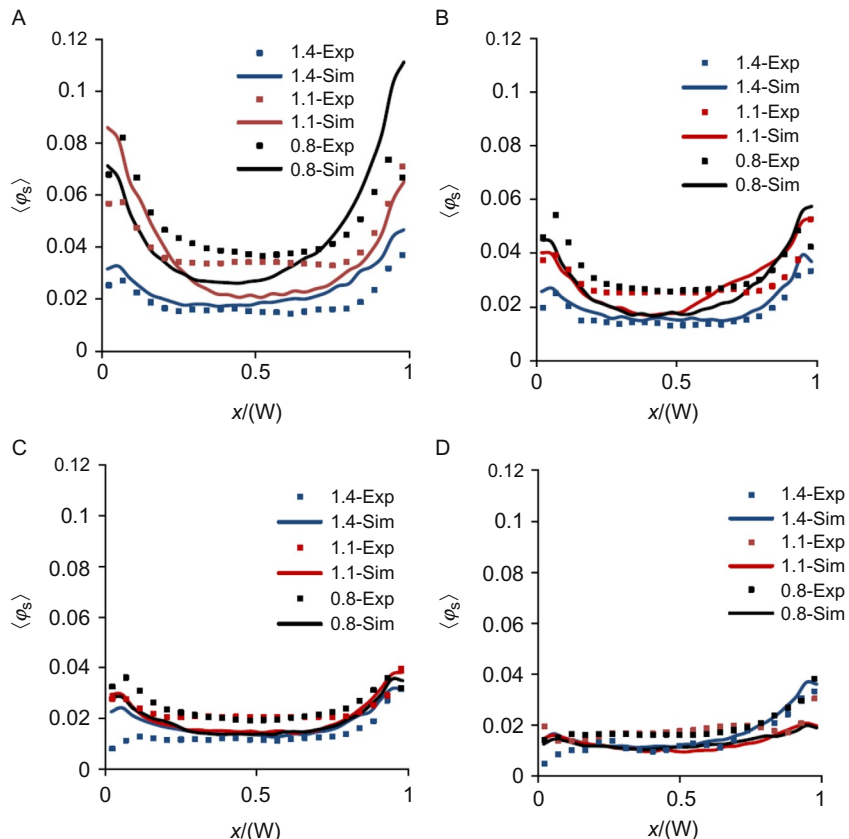


Fig. 11 Experimental and simulated lateral profiles of the time-averaged solids volume fraction at several heights in the riser for several superficial gas velocities. (A) $u_o = 5.55$ m/s, (B) $u_o = 5.95$ m/s, (C) $u_o = 6.35$ m/s, and (D) $u_o = 6.74$ m/s. Reproduced with permission from Carlos Varas AE, Peters EAJF, Kuipers JAM: CFD–DEM simulations and experimental validation of clustering phenomena and riser hydrodynamics, Chem Eng Sci 169:246–258, 2017a.

models to include more realistic particle collision models accounting for particle friction as well as tangential restitution is quite challenging and has recently been reported by Yang et al. (2016a, 2016b) together with the appropriate boundary conditions at confining solid walls. Special algorithms are required to solve the governing equations which basically extend the well-known SIMPLE algorithm (Patankar and Spalding, 1972) to the so-called p - ϵ algorithm to enable the stable integration of the governing equations with a (substantially) bigger time step (Verma et al., 2013).

The organization of this section is as follows: first the governing and constitutive equations will be presented (Section 4.1) followed by a brief

description of the numerical solution method (Section 4.2). In Section 4.3, the main results will be presented.

4.1 Governing Equations TFM

In the TFM, the concept of interpenetrating continuous media is used leading to separate conservation equations for mass, momentum, and heat for each phase (see Table 4). The main assumptions are:

- The fluid phase (gas) is compressible and obeys the ideal gas law.
- The thermophysical properties of both phases are constant.
- The solid phase can be modeled as a continuum and can be well represented by a mass density, velocity, and granular temperature field.
- Closure relations exist for intraparticle interactions (solids stress and pressure) and solid–fluid interaction (drag, transfer coefficients).

In addition to the governing equations, additional equations are required to close the set of equations. These closure equations are given in Table 5 and include equations for the interphase exchange of mass, momentum, and heat as well as closure equations for the stress tensors, fluctuating kinetic energy flux, and the transport coefficients. In addition, a closure for the dissipation

Table 4 TFM Governing Equations in Vector Form Based on the KTGF

Fluid phase continuity equation:

$$\frac{\partial}{\partial t} (\varepsilon_g \rho_g) + \nabla \cdot (\varepsilon_g \rho_g \bar{u}_g) = 0$$

Solid phase continuity equation:

$$\frac{\partial}{\partial t} (\varepsilon_s \rho_s) + \nabla \cdot (\varepsilon_s \rho_s \bar{u}_s) = 0$$

Fluid phase momentum equation:

$$\frac{\partial}{\partial t} (\varepsilon_g \rho_g \bar{u}_g) + \nabla \cdot (\varepsilon_g \rho_g \bar{u}_g \bar{u}_g) = -\varepsilon_g \nabla p_g - \nabla \cdot (\varepsilon_g \bar{\tau}_g) - \beta(\bar{u}_g - \bar{u}_s) + \varepsilon_g \rho_g \bar{g}$$

Solid phase momentum equation:

$$\frac{\partial}{\partial t} (\varepsilon_s \rho_s \bar{u}_s) + \nabla \cdot (\varepsilon_s \rho_s \bar{u}_s \bar{u}_s) = -\varepsilon_s \nabla p_g - \nabla p_s - \nabla \cdot (\varepsilon_s \bar{\tau}_s) + \beta(\bar{u}_g - \bar{u}_s) + \varepsilon_s \rho_s \bar{g}$$

Granular temperature equation:

$$\frac{3}{2} \left[\frac{\partial}{\partial t} (\varepsilon_s \rho_s \theta) + \nabla \cdot (\varepsilon_s \rho_s \theta \bar{u}_s) \right] = -\left(p_s \bar{I} + \varepsilon_s \bar{\tau}_s \right) : \nabla \bar{u}_s - \nabla \cdot (\varepsilon_s \bar{q}_s) - 3\beta\theta - \gamma$$

Fluid phase thermal energy equation:

$$C_{p,g} \left[\frac{\partial}{\partial t} (\varepsilon_g \rho_g T_g) + \nabla \cdot (\varepsilon_g \rho_g \bar{u}_g T_g) \right] = \nabla \cdot (\varepsilon_g \kappa_{g,e} \nabla T_g) - \alpha(T_g - T_s)$$

Solid phase thermal energy equation:

$$C_{p,s} \left[\frac{\partial}{\partial t} (\varepsilon_s \rho_s T_s) + \nabla \cdot (\varepsilon_s \rho_s \bar{u}_s T_s) \right] = \nabla \cdot (\varepsilon_s \kappa_{s,e} \nabla T_s) + \alpha(T_g - T_s)$$

Table 5 Two-Fluid Model, Closure Equations (Nieuwland et al., 1996)

Fluid–particle drag:

$$\beta = 18(1 - \varepsilon_g)\varepsilon_g\mu_g \frac{F}{d_p^2}$$

Ergun dimensionless drag (1952) for $\varepsilon_g < 0.8$ (Ergun, 1952):

$$F = \frac{150}{18} \frac{\varepsilon_g}{(1 - \varepsilon_g)^2} + \frac{1.75}{18} \frac{Re_p}{(1 - \varepsilon_g)^2} \quad Re_p = \frac{\varepsilon_g \rho_g |\bar{u}_g - \bar{u}_s| d_p}{\mu_g}$$

Wen and Yu dimensionless drag (1966) for $\varepsilon_g > 0.8$ (Wen and Yu, 1966):

$$F = \frac{1}{24} C_d \varepsilon_g^{-3.65} Re_p$$

$$C_d = \frac{24}{Re_p} \left(1 + 0.15 Re_p^{0.687} \right) \text{ for } Re_p < 1000 \text{ and } C_d = 0.44 \text{ for } Re_p > 1000$$

Fluid–particle heat transfer:

$$\alpha = \frac{6(1 - \varepsilon_g)}{d_p} \alpha_p$$

Gunn (1978) fluid–particle heat transfer correlation:

$$Nu_p = \frac{\alpha_p d_p}{\kappa_g} = \left(7 - 10\varepsilon_g + 5\varepsilon_g^2 \right) \left(1 + 0.7 (Re_p)^{0.2} Pr^{1/3} \right) \\ + \left(1.33 - 2.4\varepsilon_g + 1.2\varepsilon_g^2 \right) (Re_p)^{0.7} Pr^{1/3}$$

$$Pr = \frac{C_{p,g}\mu_g}{\kappa_g}$$

Solid phase pressure:

$$p_s = (1 + 2(1 + e_n)\varepsilon_g g_0)\varepsilon_s \rho_s \theta$$

Newtonian stress tensor fluid phase:

$$\bar{\tau}_g = - \left[\left(\lambda_g - \frac{2}{3}\mu_g \right) (\nabla \cdot \bar{u}_g) \bar{I} + \mu_g \left((\nabla \bar{u}_g) + (\nabla \bar{u}_g)^T \right) \right]$$

Newtonian stress tensor solid phase:

$$\bar{\tau}_s = - \left[\left(\lambda_s - \frac{2}{3}\mu_s \right) (\nabla \cdot \bar{u}_s) \bar{I} + \mu_s \left((\nabla \bar{u}_s) + (\nabla \bar{u}_s)^T \right) \right]$$

Bulk viscosity solid phase:

$$\lambda_s = \frac{4}{3} \varepsilon_s \rho_s d_p g_0 (1 + e_n) \sqrt{\frac{\theta}{\pi}}$$

Shear viscosity solid phase:

$$\mu_s = 1.01600 \frac{5}{96} \pi \rho_s d_p \sqrt{\frac{\theta}{\pi}} \left(1 + \frac{8(1 + e_n)}{5} \varepsilon_s g_0 \right) \left(1 + \frac{8}{5} \varepsilon_s g_0 \right) + \frac{4}{5} \varepsilon_s \rho_s d_p g_0 (1 + e_n) \sqrt{\frac{\theta}{\pi}} + \mu_s^f$$

Pseudo Fourier fluctuating kinetic energy flux:

$$\bar{q}_s = -\kappa_s \nabla \theta$$

Pseudothermal conductivity solid phase:

$$\kappa_s = 1.02513 \frac{75}{384} \pi \rho_s d_p \sqrt{\frac{\theta}{\pi}} \left(1 + \frac{12(1 + e_n)}{5} \varepsilon_s g_0 \right) \left(1 + \frac{12}{5} \varepsilon_s g_0 \right) + 2 \varepsilon_s \rho_s d_p g_0 (1 + e_n) \sqrt{\frac{\theta}{\pi}}$$

Continued

Table 5 Two-Fluid Model, Closure Equations ([Nieuwland et al., 1996](#))—cont'd

Dissipation rate of granular energy due to inelastic particle–particle collisions:

$$\gamma = 3(1 - \epsilon_n^2) \epsilon_s^2 \rho_s g_0 \theta \left[\frac{4}{d_p} \sqrt{\frac{\theta}{\pi}} - (\nabla \cdot \vec{u}_s) \right]$$

Radial distribution function:

$$g_0 = 1 + 4\epsilon_s \frac{1 + 2.5\epsilon_s + 4.5904\epsilon_s^2 + 4.515439\epsilon_s^3}{\left(1 - \left(\frac{\epsilon_s}{\epsilon_{s,\max}}\right)^3\right)^{0.67802}}$$

$$\epsilon_{s,\max} = 0.64356$$

Frictional stress model:

$$\mu_s^f = \frac{p_c \sqrt{2} \sin \phi}{2\epsilon_s \sqrt{(\bar{D} : \bar{D}) + \theta/d_p^2}}, \quad \bar{D} = \left(\frac{1}{2} ((\nabla \bar{u}_s) + (\nabla \bar{u}_s)^T) - \frac{1}{3} (\nabla \cdot \bar{u}_s) \bar{I} \right)$$

$$p_c = \begin{cases} F \frac{(\epsilon_s - \epsilon_{s,\min})}{(\epsilon_{s,\max} - \epsilon_{s,\min})^s} & \epsilon_s > \epsilon_{s,\min} \\ 0 & \epsilon_s < \epsilon_{s,\min} \end{cases}$$

$$F = 0.05 \text{ (N/m}^2\text{)}, \quad r = 2, \quad s = 3, \quad \epsilon_{s,\min} = 0.5, \quad \phi = 28 \text{ degree}$$

Fluid phase thermal conductivity:

$$\kappa_{g,e} = \left(\frac{1 - \sqrt{1 - \epsilon_g}}{\epsilon_g} \right) \kappa_g$$

Solid phase thermal conductivity:

$$\kappa_{s,e} = \left(\frac{\omega A + (1 - \omega)\Gamma}{\sqrt{1 - \epsilon_g}} \right) \kappa_s$$

where

$$\Gamma = \frac{2}{\left(1 - \frac{B}{A}\right)} \left(\frac{(A-1)}{\left(1 - \frac{B}{A}\right)^2 A} \ln \left(\frac{A}{B} \right) - \frac{(B-1)}{\left(1 - \frac{B}{A}\right)} - \frac{1}{2}(B+1) \right)$$

with

$$B = 1.25 \left(\frac{1 - \epsilon_g}{\epsilon_g} \right)^{10/9} \quad \text{and} \quad A = \frac{\kappa_s}{\kappa_g} \quad \omega = 0.00726$$

of granular energy due to inelastic particle–particle collisions is required as well as a closure for the so-called frictional stress model which is important in quasi-static regions of the fluidized bed where the basic assumptions underlying the KTGF break down. The KTGF reported in this chapter is mainly based on [Nieuwland et al. \(1996\)](#) and the extended model (to incorporate frictional stress models) of [Verma et al. \(2013\)](#). Finally for the solution of the complete set of equations suitable boundary conditions need to be specified at all boundaries of the computational domain. For the solid phase, the

boundary conditions for confining walls have been formulated by [Pita and Sundaresan \(1991\)](#), respectively, for the solids phase momentum equation and the granular temperature equation:

$$\left(\bar{\bar{I}} - \bar{m}\bar{n}\right)(\bar{\tau}_s \cdot \bar{n}) = \frac{\varphi\sqrt{3}\pi\varepsilon_s\rho_g g_0 \theta \bar{u}_s}{6\varepsilon_{s,\max}} \quad (52)$$

$$(\bar{q}_s \cdot \bar{n}) = \frac{\sqrt{3}\pi\varepsilon_s\rho_g g_0 \theta^{3/2} (1 - e_w^2)}{4\varepsilon_{s,\max}} - (\bar{u}_s \cdot \bar{\tau}_s \cdot \bar{n}) \quad (53)$$

4.2 Numerical Solution Method TFM

For the solution of the governing equations, a semiimplicit methodology is used described in detail in [Verma et al. \(2013\)](#). Consequently only the main features of the method will be given here starting with the time discretization of the continuity and momentum equations:

$$\left(\varepsilon_g \rho_g\right)^{n+1} = \left(\varepsilon_g \rho_g\right)^n - \Delta t \left(\nabla \cdot \varepsilon_g \rho_g \bar{u}_g\right)^{n+1} \quad (54)$$

$$\left(\varepsilon_s \rho_s\right)^{n+1} = \left(\varepsilon_s \rho_s\right)^n - \Delta t \left(\nabla \cdot \varepsilon_s \rho_s \bar{u}_s\right)^{n+1} \quad (55)$$

$$\begin{aligned} \left(\varepsilon_g \rho_g \bar{u}_g\right)^{n+1} &= \left(\varepsilon_g \rho_g \bar{u}_g\right)^n - \Delta t \left(\varepsilon_g \nabla p_g\right)^{n+1} + \bar{A}_g \\ &\quad - \Delta t \beta^n (\bar{u}_g - \bar{u}_s) + \Delta t \left(\varepsilon_g \rho_g \bar{g}\right) \end{aligned} \quad (56)$$

$$\begin{aligned} \left(\varepsilon_s \rho_s \bar{u}_s\right)^{n+1} &= \left(\varepsilon_s \rho_s \bar{u}_s\right)^n - \Delta t \left(\varepsilon_s \nabla p_g\right)^{n+1} \\ &\quad - \Delta t \left(\nabla p_s\right)^{n+1} + \bar{A}_s + \Delta t \beta^n (\bar{u}_g - \bar{u}_s) + \Delta t \left(\varepsilon_s \rho_g \bar{g}\right) \end{aligned} \quad (57)$$

where n represents the time index whereas \bar{A}_g and \bar{A}_s contain, respectively, the convective and viscous contributions for the gas phase and solid phase. For the spatial discretization, a uniform staggered computational grid is used where the scalar variables are defined at the cell centers whereas the velocity components are defined at the cell faces.

The viscous contributions are treated with a mixed explicit–implicit scheme where the normal and mixed derivatives are treated, respectively, implicitly and explicitly. In the first step of the solution procedure intermediate momentum densities are computed for both phases on basis of the following two equations where the pressure and interphase momentum exchange terms in Eqs. [\(56\)](#) and [\(57\)](#) are excluded:

$$\left(\varepsilon_g \rho_g \bar{u}_g\right)^{**} = \left(\varepsilon_g \rho_g \bar{u}_g\right)^n + \bar{A}_{g,\text{con+vis}}^{**} + \bar{A}_{g,\text{con+vis}}^n + \Delta t \left(\varepsilon_g \rho_g \bar{g}\right) \quad (58)$$

$$\left(\varepsilon_s \rho_s \bar{u}_s\right)^{**} = \left(\varepsilon_s \rho_s \bar{u}_s\right)^n + \bar{A}_{s,\text{con+vis}}^{**} + \bar{A}_{s,\text{con+vis}}^n + \Delta t \left(\varepsilon_s \rho_g \bar{g}\right) \quad (59)$$

The convective contributions are treated with the deferred correction approach where the convective fluxes are written as follows:

$$\begin{aligned} A_{g,\text{con}}^{**} &= \bar{A}_{g,\text{con},\text{UPW}}^{n+1} + \left(\bar{A}_{g,\text{con},\text{TVD}}^n - \bar{A}_{g,\text{con},\text{UPW}}^n \right) \\ A_{s,\text{con}}^{**} &= \bar{A}_{s,\text{con},\text{UPW}}^{n+1} + \left(\bar{A}_{s,\text{con},\text{TVD}}^n - \bar{A}_{s,\text{con},\text{UPW}}^n \right) \end{aligned} \quad (60)$$

where the lower-order upwind (UPW) part is treated implicitly whereas the higher-order part (based on total variation diminishing (TVD)) is treated explicitly. This approach contributes to the main diagonal dominance of the algebraic equations and provides a stable solution with better convergence characteristics. Subsequently these intermediate momentum densities are corrected by solving the following two equations:

$$\left(\varepsilon_g \rho_g \bar{u}_g \right)^{n+1} = \left(\varepsilon_g \rho_g \bar{u}_g \right)^{**} - \Delta t (\varepsilon_g \nabla p_g)^{n+1} - \Delta t \beta^n (\bar{u}_g - \bar{u}_s) \quad (61)$$

$$\begin{aligned} (\varepsilon_s \rho_s \bar{u}_s)^{n+1} &= (\varepsilon_s \rho_s \bar{u}_s)^{**} - \Delta t (\varepsilon_s \nabla p_g)^{n+1} \\ &\quad - \Delta t (\nabla p_s)^{n+1} + \Delta t \beta^n (\bar{u}_g - \bar{u}_s) \end{aligned} \quad (62)$$

where the advanced time level pressure and solids volume fraction are computed from the following two equations for the respective corrections:

$$\begin{aligned} & (J_g)_{i-1,j,k}^n (\Delta p_g)_{i-1,j,k}^{n+1} + (J_g)_{i+1,j,k}^n (\Delta p_g)_{i+1,j,k}^{n+1} + (J_g)_{i,j-1,k}^n (\Delta p_g)_{i,j-1,k}^{n+1} \\ & + (J_g)_{i,j+1,k}^n (\Delta p_g)_{i,j+1,k}^{n+1} + (J_g)_{i,j,k-1}^n (\Delta p_g)_{i,j,k-1}^{n+1} \\ & + (J_g)_{i,j,k+1}^n (\Delta p_g)_{i,j,k+1}^{n+1} + (J_g)_{i,j,k}^n (\Delta p_g)_{i,j,k}^{n+1} = -(D_g)_{j,j,k}^{n+1} \end{aligned} \quad (63)$$

$$\begin{aligned} & (J_s)_{i-1,j,k}^n (\Delta \varepsilon_s)_{i-1,j,k}^{n+1} + (J_s)_{i+1,j,k}^n (\Delta \varepsilon_s)_{i+1,j,k}^{n+1} + (J_s)_{i,j-1,k}^n (\Delta \varepsilon_s)_{i,j-1,k}^{n+1} \\ & + (J_s)_{i,j+1,k}^n (\Delta \varepsilon_s)_{i,j+1,k}^{n+1} + (J_s)_{i,j,k-1}^n (\Delta \varepsilon_s)_{i,j,k-1}^{n+1} + (J_s)_{i,j,k+1}^n (\Delta \varepsilon_s)_{i,j,k+1}^{n+1} \\ & + (J_s)_{i,j,k}^n (\Delta \varepsilon_s)_{i,j,k}^{n+1} = -(D_s)_{j,j,k}^{n+1} \end{aligned} \quad (64)$$

where J_g and J_s represent the Jacobi matrices for, respectively, the gas and solid phase which are evaluated at the old time level. These matrices contain the derivatives of the mass residuals D_g and D_s according to the continuity equations of the gas and solid phase with respect to the pressure and solids volume fraction, respectively, and can be obtained analytically from the continuity and momentum equations. Effectively the solution method constitutes a two-step projection method combined with an extension of the SIMPLE algorithm of Patankar and Spalding (1972).

Once the corrections for the pressure and solids volume fraction have been obtained from Eqs. (63) and (64), Eqs. (61) and (62) can be solved to obtain new estimates of the advanced time level momentum densities and updated values of the mass residuals D_g and D_s . This process is continued until the mass residuals satisfy the imposed convergence criteria. Following the solution of the continuity and momentum equations, the granular temperature equation is solved by an iterative procedure. Following the solution of the hydrodynamic equations, the thermal energy equations are solved using a fully implicit scheme. The resulting linear set of equations for the intermediate momentum densities (Eqs. 58 and 59), the pressure and solids volume fraction corrections (Eqs. 63 and 64), the discretized granular temperature equation, and the coupled thermal energy equations (see Table 4) are all solved with a sparse matrix solver based on the ICGM.

4.3 Results TFM

In this section, illustrative computational results will be presented highlighting the capabilities of continuum modelling of dense gas–fluidized beds with focus on the hydrodynamics (gas bubbles behavior, solids motion, and mixing and heat transfer). In Section 4.3.1, we will focus on pseudo 2D beds whereas in Section 4.3.2, we will focus on 3D cylindrical beds. Finally in Section 4.3.3, we will focus on nonisothermal systems involving a 3D cylindrical gas–fluidized with heat production in the solid phase.

4.3.1 Hydrodynamics of a Pseudo 2D Gas–Fluidized Bed

Pseudo 2D gas–fluidized beds have been used extensively to study in detail the hydrodynamics because the complex behavior of the rising gas bubbles and associated solids motion can be monitored with relative ease using powerful noninvasive optical techniques such as DIA and PIV. In Fig. 12, we show the bubble formation and propagation computed from the TFM governing equations for a pseudo 2D gas–fluidized bed with a central jet. The data used for this simulation are given in Table 6.

The simulation results reveal a complex pattern of bubble formation with rapid growth of the bubbles due to strong vertical coalescence of the detached bubbles. A similar pattern is observed in experiments and it has been shown that the initial bubble size and time–averaged porosity distribution obtained from similar computations agree reasonably well with experimental data obtained for such pseudo 2D gas–fluidized beds (see, respectively, Kuipers et al., 1991, 1992a). These studies also revealed that during the initial stage of bubble formation at an orifice substantial leakage

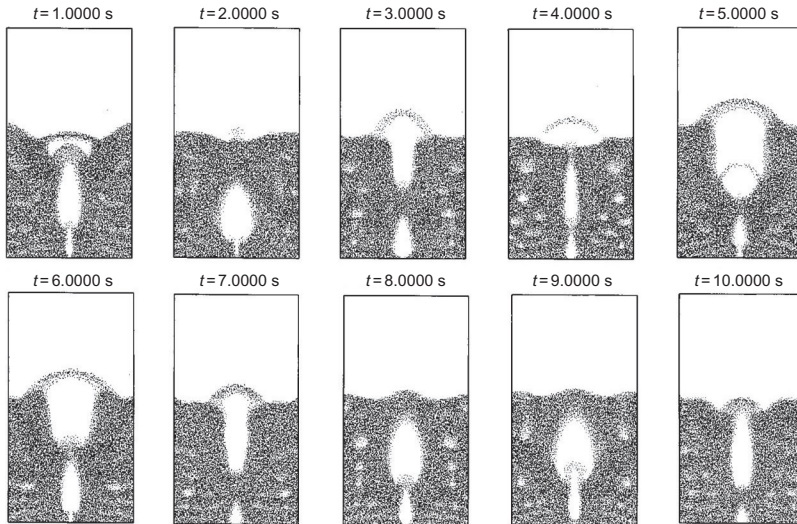


Fig. 12 Bubble formation and propagation in a 2D gas-fluidized bed with a central jet. See Table 3 for the data used in the simulation. Visualization of the porosity distribution is done with “dot plots” where the number of dots plotted for a specific computational cell is proportional to the solids volume fraction. For cells with a solids volume fraction less than 0.15 no dots are distributed.

Table 6 Data Used for the Numerical Simulation of Bubble Formation and Propagation in a Pseudo 2D Gas-Fluidized Bed With a Central Jet

Gas density	Ideal gas law	kg/m^3
Gas viscosity	2.0×10^{-5}	$\text{kg}/(\text{m s})$
Particle size	500	μm
Particle density	2660	kg/m^3
Restitution coefficient	0.95	(–)
Time step	10^{-4}	s
Bed dimensions	0.570 (<i>x</i> -direction) 0.015 (<i>y</i> -direction) 1.000 (<i>z</i> -direction)	
Computational grid size and number of computational cells	0.0075 (<i>x</i> -direction) (76 cells) 0.0075 (<i>y</i> -direction) (2 cells) 0.0100 (<i>z</i> -direction) (100 cells)	
Background velocity	0.25	m/s
Jet velocity	10.0	m/s

of the gas injected through the orifice into the emulsion phase occurs which is particularly important in case fast heterogeneously catalyzed reactions take place.

With the advent of powerful optical measuring techniques such as DIA and PIV the solids motion in such systems could be studied in detail as well and is shown in Fig. 13. In this figure, the time-averaged filtered emulsion phase velocity measured in a bed with a width of 0.30 m and a packed height of 0.30 m is shown for several fluidization velocities.

The combined usage of DIA and PIV allows to correct for the influence of particle raining through the roof of the bubbles on the time-averaged emulsion phase velocities (Laverman et al., 2008). From this figure, it can be seen that the solids motion is quite complex with circulation cells in the top part of the bed where the strength of the circulation cells depends strongly on the fluidization velocity. In the center of the bed the particles flow upward due to the strong bubble propagation in this part of the bed, while the particles flow downward near the confining walls. These datasets have been used extensively to validate both DEM and TFM models for gas-fluidized beds.

4.3.2 Hydrodynamics of a 3D Cylindrical Bed

In the previous section, the focus was on pseudo 2D gas-fluidized beds which feature many important properties of real (complex) 3D gas-fluidized beds. However, gas-fluidized beds encountered in the process industries typically possess a cylindrical geometry which introduces an additional degree of freedom for bubble propagation and solids motion. Moreover, internals immersed in the fluidized solids might be present to facilitate efficient heat removal from the bed in case strongly exothermic catalyzed reactions occur. Finally multiple inlets for the gas and/or solids phase might exist to enable continuous and flexible operation (see Fig. 1).

The treatment of the boundary condition at the center of the bed requires a special procedure detailed in Verma et al. (2013) to avoid artificial accumulation of solids near the center line of the bed. As an alternative to solving the TFM conservation equations in full 3D cylindrical coordinates these equations can be solved as well on curvilinear coordinates (Manger, 1996) or on regular Cartesian grids where the cylindrical wall is treated with the IBM. See the excellent review paper by Mittal and Iaccarino (2005) for a more detailed discussion of the latter technique.

Verma et al. (2013) also studied the effect of the discretization scheme for the convection terms and recommended to use high-order schemes such as

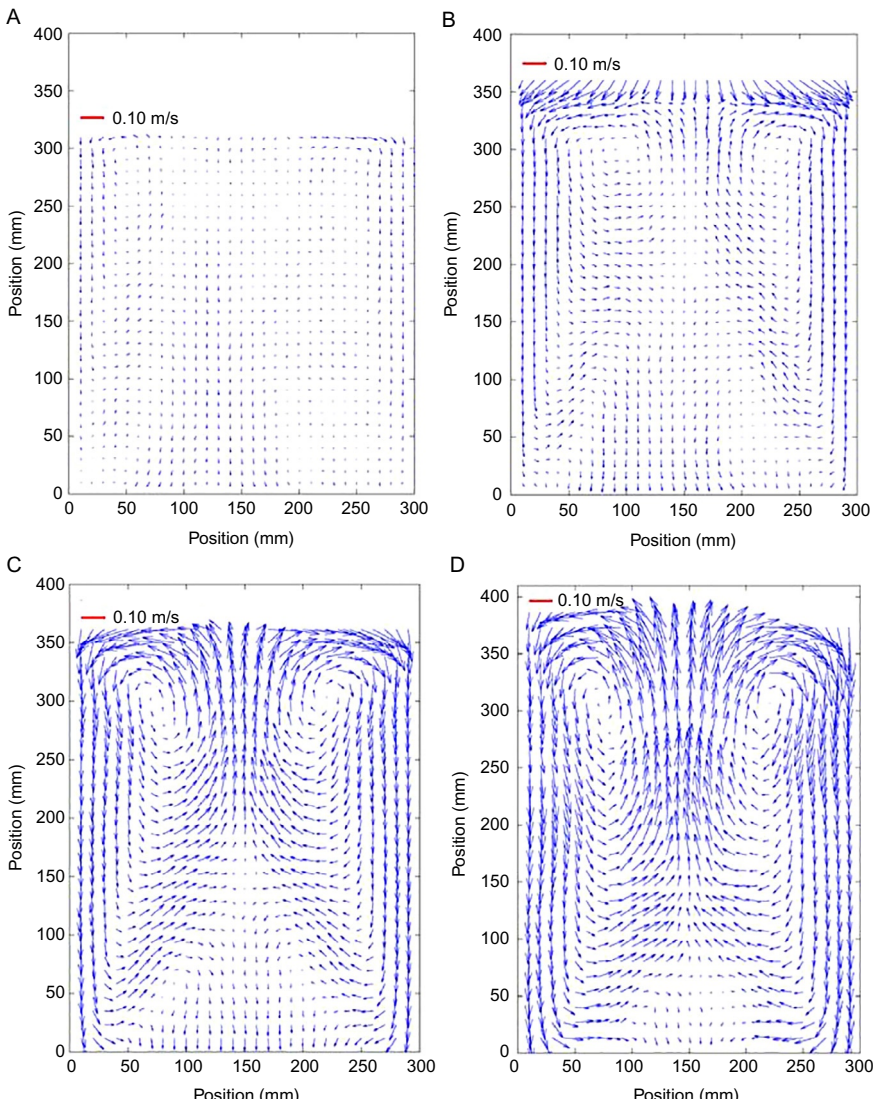


Fig. 13 Time-averaged filtered emulsion phase velocity profiles measured in a bed with a width of 0.30 m and a packed bed ratio of 1.0 for several fluidization velocities: (A) $(u_0/u_{mf}) = 1.5$, (B) $(u_0/u_{mf}) = 2.0$, (C) $(u_0/u_{mf}) = 2.5$, and (D) $(u_0/u_{mf}) = 3.5$. Glass bead in the size range of 400–600 μm (Geldart B-type) were used in these experiments using air as fluidizing agent. Reproduced with permission from Laverman JA, Roghair I, van Sint Annaland M, Kuipers JAM: Investigation into the hydrodynamics of gas–solid fluidized beds using particle image velocimetry coupled with digital image analysis, Can J Chem Eng 86:523–535, 2008.

TVD schemes instead of the first-order upwind (FOU) scheme to avoid excessive numerical diffusion or “computational smearing.” This is especially important to capture the small bubbles formed in the bottom zone of the bed. Moreover, for dense gas-fluidized beds with heterogeneously catalyzed reactions the preservation of sharp boundaries between gas bubbles and the dense emulsion phase is of crucial importance to correctly predict the degree of chemical conversion in case fast reactions proceed. The data used for the numerical simulation of a freely bubbling 3D cylindrical bed are summarized in [Table 7](#). In [Fig. 14](#), we show instantaneous snapshots of the volume fraction of the gas in the central plane of a 3D 0.306 m diameter gas-fluidized bed revealing a dynamic evolution of a very complex void structure.

From [Fig. 14](#), it can be seen that the small bubbles that form near the gas distributor plate rapidly coalesce to form larger bubbles at a higher elevation in the bed. From animations of this process, it can clearly be seen that these large bubbles tend to rise in the center of the bed. This pattern of bubble propagation is well known and leads to a large-scale circulation pattern in the bed with solids up-flow in the central portion of the bed and solids down-flow near the cylindrical wall of the bed.

Table 7 Data Used for the Numerical Simulation of a Freely Bubbling 3D Cylindrical Dense Gas-Fluidized Bed

Gas density	Ideal gas law	kg/m ³
Gas viscosity	2.0×10^{-5}	kg/(m s)
Particle size	500	μm
Particle density	2500	kg/m ³
Restitution coefficient	0.86	(–)
Time step	10^{-4}	s
Bed dimensions	0.306 (radial direction) 1.000 (axial direction)	m m
Computational grid	45 (radial direction) 30 (azimuthal direction) 240 (axial direction)	(–) (–) (–)
Minimum fluidization velocity U_{mf}	0.18	m/s
Superficial gas velocity	$3.5U_{mf}$	m/s

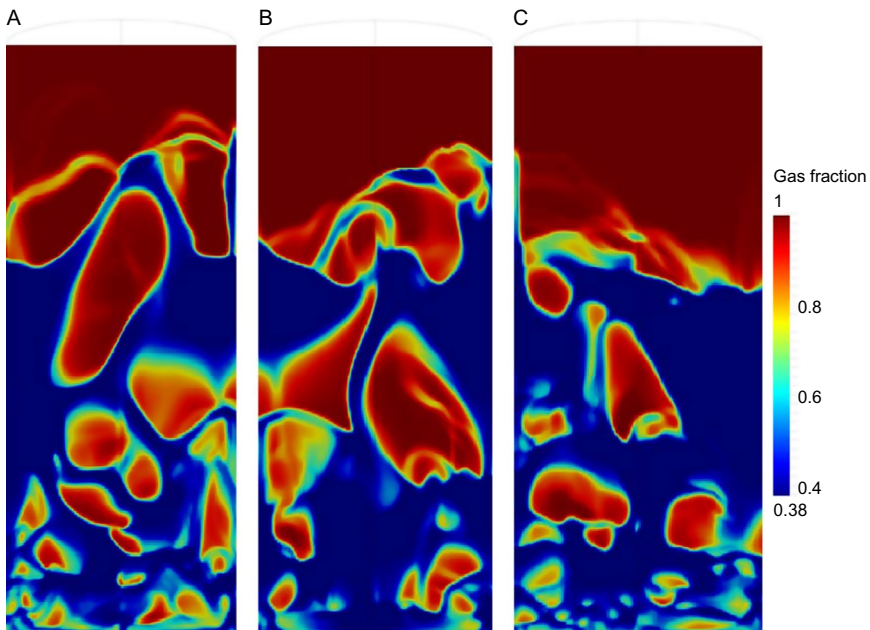


Fig. 14 Instantaneous snapshots of the volume fraction of gas in the central plane of a 3D 0.306 m diameter gas-fluidized bed at $t = 2.6$ s (A), $t = 4.0$ s (B), and $t = 5.0$ s (C). The simulation settings are given in Table 7. Reproduced with permission from Verma V, Deen NG, Padding JT, Kuipers JAM: Two-fluid modelling of three-dimensional cylindrical gas–solid fluidized beds using the kinetic theory of granular flow, Chem Eng Sci 102:227–245, 2013.

This pattern of solids motion is also found experimentally and as an example we show in Fig. 15, the azimuthally and time-averaged solids circulation pattern obtained from experiments (Laverman et al., 2012) and TFM simulations. The experimental results were obtained with a positron emission particle tracking (PEPT) technique in which the position of an activated particle was measured as a function of time over a sufficiently long measuring time. Inspection of Fig. 15 reveals the presence of two circulation cells, one in the bottom portion of the bed and a larger cell in the upper portion of the bed. The main features of the experimentally found solids circulation pattern are very well reproduced by the TFM simulations. Verma et al. (2015) also studied the effect of bed size and aspect ratio on the hydrodynamics in 3D gas–solid fluidized beds with Geldart B-type particles and found that the bubble size closely follows the empirical correlation proposed by Werther (1976) for small beds and the correlation proposed by Darton et al. (1977) for sufficiently large beds. They also found that the bubble size

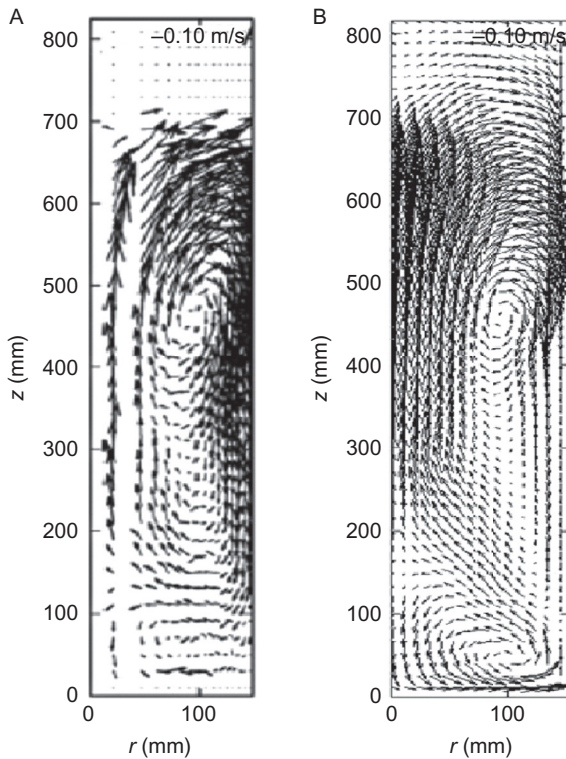


Fig. 15 Azimuthally and time-averaged solids circulation pattern obtained from experiments using PEPT ([Laverman et al., 2012](#)) and TFM simulations. See [Table 7](#) for the data used in the simulation. Reproduced with permission from Verma V, Deen NG, Padding JT, Kuipers JAM: Two-fluid modelling of three-dimensional cylindrical gas–solid fluidized beds using the kinetic theory of granular flow, *Chem Eng Sci* 102:227–245, 2013.

increases when the bed diameter is increased from 0.10 to 0.30 m diameter and remains approximately constant for bed diameters ranging from 0.30 to 1.0 m. For the largest bed diameter of 1.0 m, they found an increase in the bubble rise velocity which was attributed to the so-called Gulf Stream circulation which becomes important for large diameter beds ([Matsen, 1996](#)). This phenomenon leads to a concentration of the gas bubbles in the center of the bed and significantly affects the rise velocity of the bubbles.

The empirical correlations of [Werther \(1976\)](#) and [Darton et al. \(1977\)](#) are based on point measurements using so-called probe techniques. Such measurements are very time consuming and as such TFM simulations provide an attractive alternative to obtain data on bubble size. [Verma et al.](#)

(2015) also found a pronounced difference in shallow and deep beds with respect to the bubble size and solids circulation patterns which is expected behavior in view of the opportunity of the rising gas bubbles to coalesce.

Besides the comparison of the simulated bubble size with data obtained from well-established correlations, Verma et al. (2014b) also compared their simulation results on bubble dynamics in a 3D gas-fluidized bed with experimental data obtained using ultrafast electron beam X-ray tomography and reported good agreement between the bubble sizes obtained from experiments and TFM simulations as shown in Fig. 16.

Verma et al. (2014a) also studied the effect of operating pressure on the hydrodynamics of a 0.30 m diameter gas-fluidized bed containing 1.1 mm diameter LLDPE particles using a constant excess gas velocity. They found a substantial effect of pressure on bubble size and shape (up to 8 bar for shape), pressure fluctuations, the time-averaged porosity distribution, and the solids circulation pattern. They reported that the bubble size decreases with increasing operating pressure and that the distinct two-phase flow structure becomes less pronounced with increasing pressure. In other words, these results indicate that gradually the heterogeneous flow structure disappears with increasing operating pressure. In Fig. 17, we show the PDF of the time-averaged porosity distribution for several heights in the bed at atmospheric pressure (left) and an elevated pressure of 20 bar (right). It can clearly be seen that the PDF becomes flatter with increasing pressure where the prevalence of intermediate porosity values (i.e., ranging from 0.6 to 0.8) is clearly noticeable.

4.3.3 Gas-Fluidized Bed With Heat Production

In many processes involving gas-fluidized beds the solid phase acts as a heterogeneous catalyst where significant heat effects play a role. Combustion, gasification, and gas phase polymerization for the production of polyolefines can be mentioned as specific examples. In the latter process, the monomer (ethylene or propylene) is contacted with a prepolymerized particles containing metallocene type of catalysts leading to rapid growth of the particles with liberation of a large amount of heat due to the strongly exothermic polymerization reactions. In this type of application, it is particularly important to avoid excessive local heating of the polymer particles (hot spot formation) because it could lead to the formation of large agglomerates causing massive defluidization and necessary shutdown of the process. The experimental investigation of such systems is very complicated and costly and as such (validated) hydrodynamic models of gas-fluidized beds

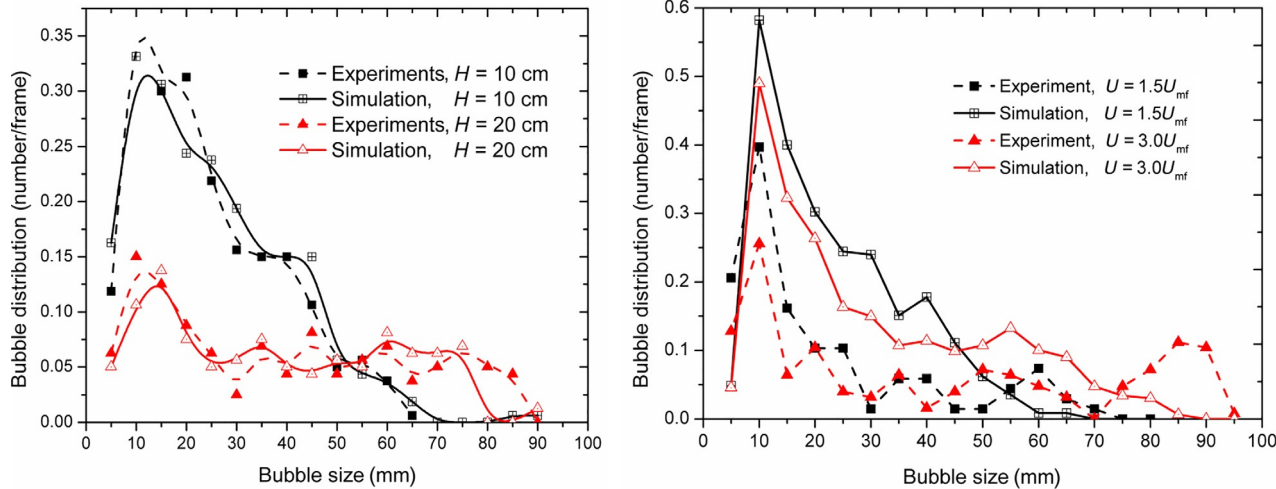


Fig. 16 Comparison of bubble size distributions computed by TFM and measured by X-ray tomography. (Left) LLDPE particles at an inlet gas velocity of $1.5 U_{mf}$ two height. (Right) Alumina particles at a height of 10 cm for two gas inlet velocities. Reproduced with permission from Verma V, Padding JT, Deen NG, Kuipers JAM, Barthel F, Bieberle M, Wagner M, Hampel U: Bubble dynamics in a 3D gas–solid fluidized bed using ultrafast electron beam X-ray tomography and two-fluid model, AIChE J 60(5):1632–1644, 2014b.

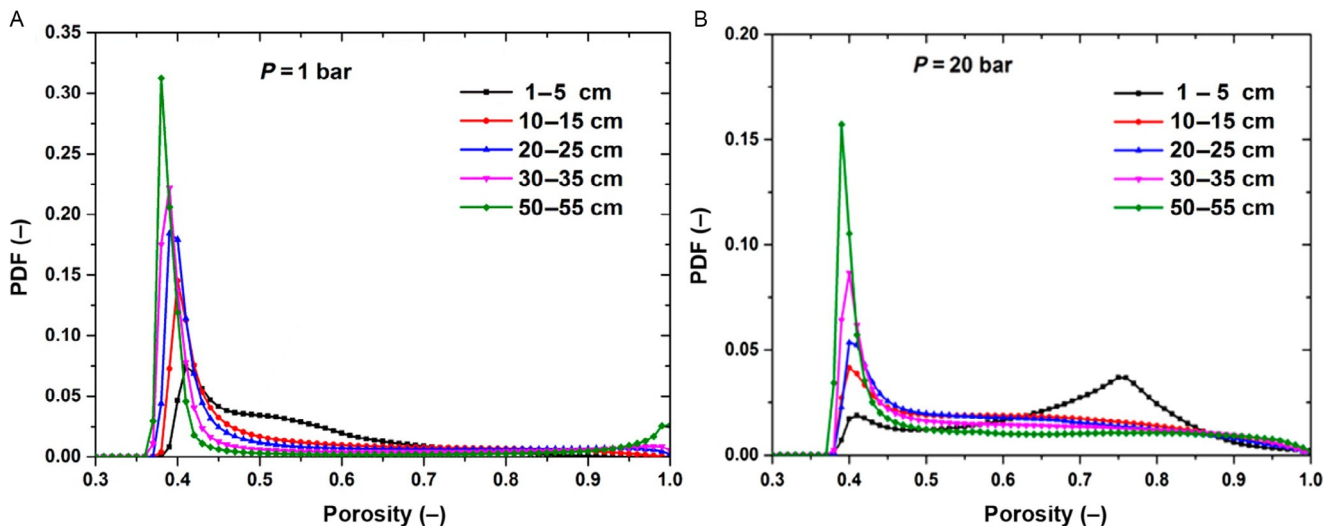


Fig. 17 PDF of the time-averaged porosity distribution for several heights in the bed at atmospheric pressure (A) and an elevated pressure of 20 bar (B). Bed and particle diameter: 0.30 m and 1.1 mm. *Reproduced with permission from Verma V, Padding JT, Deen NG, Kuipers JAM: Numerical investigation on the effect of pressure on fluidization in a 3D fluidized bed, I&EC Res 53:17487–17498, 2014a.*

supplemented with thermal energy equations offer an attractive alternative to study the complex thermal behavior.

Banaei et al. (2017) modified the thermal energy equation for the solid phase to account for the heat production in the particles by including a constant volumetric heat source (see Table 4). The value of this source was estimated from conditions which typically are encountered in gas phase polymerization processes (see Table 8). Following a careful verification of their model using both analytical solutions for unsteady 1D heat conduction with heat production and results from independent numerical solutions obtained for transient heat transfer in a fixed bed with heat production, they studied the thermal behavior of gas–fluidized beds with heat production.

Table 8 Data Used for the Numerical Simulation of a Gas–Fluidized Bed With Heat Production in the Solid Phase

Gas density	Ideal gas law	kg/m ³
Molar weight of gas	42.08	kg/kmol
Gas viscosity	1.0×10^{-5}	kg/(m s)
Gas thermal conductivity	0.0209	W/(m K)
Gas heat capacity	1670.0	J/(kg K)
Gas inlet temperature	324.0	K
Particle size	0.9875	mm
Particle density	667.0	kg/m ³
Particle–particle restitution coefficient	0.60	(–)
Particle–wall restitution coefficient	0.93	(–)
Specularity coefficient	0.50	(–)
Solid thermal conductivity	1.04	W/(m K)
Solid heat capacity	1670.0	J/(kg K)
Solid volumetric heat production rate	6.7×10^5	W/m ³
Time step	2.0×10^{-6}	s
Bed dimensions	0.06 (radial direction) 0.24 (axial direction)	m m
Computational grid	6 (radial direction) 32 (azimuthal direction) 48 (axial direction)	(–) (–) (–)

Building on the hydrodynamic model developed and validated by Verma et al. (2013, 2014a, 2014b, 2015) they studied the effect of superficial gas velocity on the solid temperature distribution in gas-fluidized beds with heat production in the context of gas phase polymerization of olefins. The data used for the numerical simulations are given in Table 8. The initial conditions for the thermal energy equations were determined by assuming that the gas-fluidized bed behaves like a continuously stirred tank reactor (CSTR). This approach avoids performing very time-consuming TFM simulations that would otherwise be required to reach the thermal steady state of the system.

In Fig. 18, we show the effect of superficial gas velocity on the solid temperature distribution in the bed revealing a rather narrow distribution where the average and spread of the distribution decreases with increasing superficial velocity. These results indicate that the temperature of the solid phase becomes more uniform with increasing superficial gas velocity due to the increased bubble-induced agitation of the solid phase.

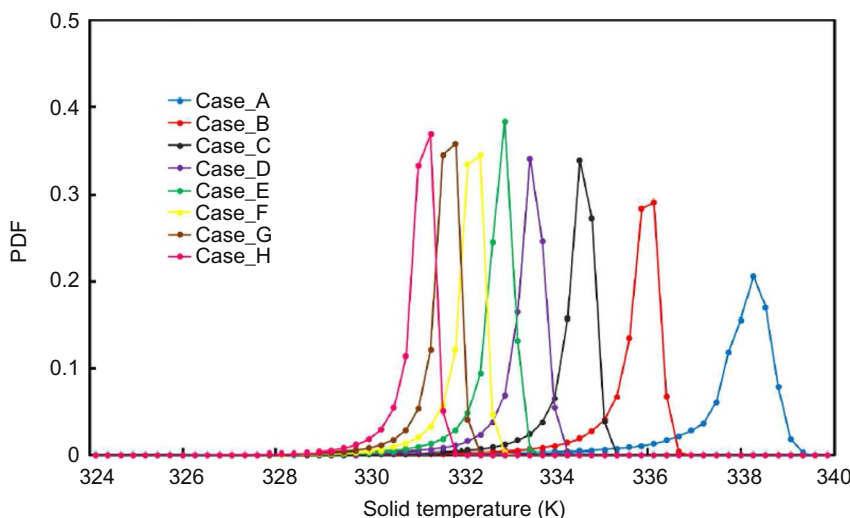


Fig. 18 Effect of superficial gas velocity on the solid temperature distribution. Case_A: $U_0 = 0.4 \text{ m/s}$, Case_B: $U_0 = 0.5 \text{ m/s}$, Case_C: $U_0 = 0.6 \text{ m/s}$, Case_D: $U_0 = 0.7 \text{ m/s}$, Case_E: $U_0 = 0.8 \text{ m/s}$, Case_F: $U_0 = 0.9 \text{ m/s}$, Case_G: $U_0 = 1.0 \text{ m/s}$, and Case_H: $U_0 = 1.1 \text{ m/s}$. See Table 8 for the data used in the simulations. Reproduced with permission from Banaei M, Jegers J, van Sint Annaland M, Kuipers JAM, Deen NG: Effect of superficial gas velocity on the solid temperature in gas fluidized beds with heat production, I&EC Res 56:8729–8737, 2017.



5. CONCLUSIONS AND OUTLOOK

In this chapter, the multiscale modelling approach of dense gas–particle flows has been discussed. These flows are extremely complex due to the fact that phenomena need to be considered which prevail over a wide range of time and length scales.

Dense gas–particle flows are frequently encountered in large-scale industrial processes involving granulation, coating, and production of base chemicals and polymers. Both (effective) fluid–particle and (dissipative) particle–particle interaction need to be accounted for because these phenomena and their mutual competition govern the key features of dense gas–fluidized beds such as the occurrence of (large-scale) heterogeneous flow structures which have a profound impact on the performance of dense gas–fluidized bed reactors.

In this chapter, it has been shown that DNS offers a viable alternative in comparison to extensive and time-consuming experimentation to obtain closures for the exchange of mass, momentum, and heat in dense gas–particle flows. The availability of such closures is of vital importance for the accurate simulation of dense particle laden flows using DEM and full continuum models. Despite the fact that considerable progress has been made in recent years enormous challenges remain to expand the multiscale approach to systems involving more complex physics. Systems involving poly-disperse dense gas–particle flows have received very limited attention so far. First of all, accurate closures for the exchange of mass, momentum, and heat are not available for dense gas–particle flows and here DNS offers a lot of potential. In addition, further development of CFD–DEM models for nonspherical particles (including particulates with sharp edges) is highly desired.

Modern continuum models of gas–fluidized beds are based on the KTGF which can be considered as a generalization of the theoretical framework underlying the “classical” continuum model for dense gas–particle flow originally proposed by [Anderson and Jackson \(1967\)](#). The governing equations have been presented together with the closure equations and the main features of the numerical solution method. For KTGF-based continuum models, further developments are necessary to include tangential friction as well as the development of efficient computational schemes to solve the strongly coupled highly nonlinear equations. Recently [Yang et al. \(2016a, 2016b\)](#) extended the “classical” TFM based on the KTGF to include

tangential friction for particle–particle collisions as well as particle–wall collisions (Yang et al., 2017b) and validated their model using magnetic particle tracking experiments and discrete particle simulations (Yang et al., 2017a). Moreover the incorporation of tangential friction in multifluid models (Manger, 1996; Van Sint Annaland et al., 2009a, 2009b) is needed.

In certain applications, such as coating, granulation, and gas phase polymerization so-called wet collisions occur which are strongly dissipative. The extension of the KTGF-based continuum models to such systems poses a big challenge since the KTGF framework relies on the prevalence of “slightly inelastic collisions.” Finally extensions are required to include simultaneous intraparticle transport of species and heat accompanied by physical and/or chemical transformations.

ACKNOWLEDGMENTS

The authors would like to acknowledge the European Research Council (ERC) for its generous financial support, under its Advanced Investigator Grant scheme, contract number 247298 (MultiScaleFlows).

REFERENCES

- Anderson TB, Jackson R: A fluid mechanical description of fluidized beds, *Ind Eng Chem Fundamen* 6:527–534, 1967.
- Banaei, M., Jegers, J., van Sint Annaland, M., Kuipers, J.A.M. and Deen, N.G., 2017, Effect of superficial gas velocity on the solid temperature in gas fluidized beds with heat production *Ind Eng Chem Res*, 56, pp 8729–8737.
- Bird RB, Stewart WE, Lightfoot EN: *Transport phenomena*, UK, 1960, John Wiley & Sons.
- Buck B, Tang Y, Heinrich S, Deen NG, Kuipers JAM: Collision dynamics of wet solids: rebound and rotation, *Powder Technol* 316:218–224, 2017.
- Carlos Varas AE, Peters EAJF, Deen NG, Kuipers JAM: Solids volume fraction measurements on riser flow using a temporal-histogram based DIA method, *AICHE J* 62(8):2681–2698, 2016.
- Carlos Varas AE, Peters EAJF, Kuipers JAM: CFD–DEM simulations and experimental validation of clustering phenomena and riser hydrodynamics, *Chem Eng Sci* 169:246–258, 2017a.
- Carlos Varas AE, Peters EAJF, Kuipers JAM: Computational fluid dynamics—discrete element method (CFD–DEM) study of mass transfer mechanisms in riser flow, *Ind Eng Chem Res* 56:5558–5572, 2017b.
- Centrella J, Wilson J: Planar numerical cosmology. II. The difference equations and numerical tests, *Astrophysical J Suppl Ser* 54:229, 1984.
- Darton RC, La Naeza RD, Davidson JF, Harrison D: Bubble growth due to coalescence in fluidized beds, *Trans Inst Chem Eng* 55:274–280, 1977.
- Das S, Deen NG, Kuipers JAM: Direct numerical simulation for flow and heat transfer through random open-cell solid foams: development of an IBM based CFD model, *Catal Today* 273:140–150, 2016.
- Das S, Deen NG, Kuipers JAM: A DNS study of flow and heat transfer through slender fixed-bed reactors randomly packed with particles, *Chem Eng Sci* 160:1–19, 2017.

- Davidson JF: Symposium on fluidization—discussion, *Trans Inst Chem Eng* 39:230–232, 1961.
- Deen NG, Kuipers JAM: Direct numerical simulation of fluid flow and mass transfer in dense fluid–particle systems, *Ind Eng Chem Res* 52:11266–11274, 2013.
- Deen NG, Kuipers JAM: Direct numerical simulation of fluid flow accompanied by coupled mass and heat transfer in dense fluid–particle systems, *Chem Eng Sci* 116:645–656, 2014.
- Deen NG, van Sint Annaland M, van der Hoef MA, Kuipers JAM: Review of discrete particle modelling of fluidized beds, *Chem Eng Sci* 62:28–44, 2007.
- Deen NG, Kriebitzsch SHL, van der Hoef MA, Kuipers JAM: Direct numerical simulation of flow and heat transfer in dense fluid–particle systems, *Chem Eng Sci* 81:329–344, 2012.
- Deen NG, Peters EAJF, Padding JT, Kuipers JAM: Review of direct numerical simulation of fluid–particle mass, *Chem Eng Sci* 116:710–724, 2014.
- Ding J, Gidaspow D: A bubbling fluidization model using kinetic theory of granular flow, *AIChE J* 36(4):523–538, 1990.
- Ergun S: Fluid flow through packed columns, *Chem Eng Progress* 48:89–94, 1952.
- Gidaspow D: Hydrodynamics of fluidization and heat transfer, *Appl Mech Rev* 39(1):1–23, 1986.
- Gunn DJ: Transfer of mass and heat to particles in fixed and fluidized beds, *Int J Heat Mass Transf* 21:467–476, 1978.
- Hoomans BPB: *Granular dynamics of gas–solid two-phase flows*, PhD Thesis, The Netherlands, 2000, Twente University.
- Hoomans BPB, Kuipers JAM, Briels WJ, Van Swaaij WPM: Discrete particle simulation of bubble and slug formation in a two-dimensional gas-fluidised bed: a hard-sphere approach, *Chem Eng Sci* 51(1):99–118, 1996.
- Kuipers JAM, Prins W, van Swaaij WPM: Theoretical and experimental bubble formation at a single orifice in a two-dimensional gas-fluidized bed, *Chem Eng Sci* (11):2881–2894, 1991.
- Kuipers JAM, Tammes H, Prins W, van Swaaij WPM: Experimental and theoretical porosity profiles in a two-dimensional gas-fluidized bed with a central jet, *Powder Technol* 71:87–99, 1992a.
- Kuipers JAM, van Duijn KJ, van Beckum FPH, van Swaaij WPM: A numerical model of gas-fluidized beds, *Chem Eng Sci* (8):1913–1924, 1992b.
- Kunii D, Levenspiel O: *Fluidization engineering*, ed 2, 1991, Butterworth-Heinemann, ISBN: 9780409902334.
- Laverman JA, Roghair I, van Sint Annaland M, Kuipers JAM: Investigation into the hydrodynamics of gas–solid fluidized beds using particle image velocimetry coupled with digital image analysis, *Can J Chem Eng* 86:523–535, 2008.
- Laverman JA, Fan X, Ingram A, et al: Experimental study on the influence of bed material on the scaling of solids circulation patterns in 3D bubbling gas–solid fluidized beds of glass and polyethylene using positron emission particle tracking, *Powder Technol* 224:297–305, 2012.
- Li Z, Janssen TCE, Buist KA, Deen NG, van Sint Annaland M, Kuipers JAM: Experimental and simulation study of heat transfer in fluidized beds with heat production, *Chem Eng J* 317:242–257, 2017.
- Lu J, Das S, Peters EAJF, Kuipers JAM: Direct numerical simulation of flow and mass transfer in dense fluid–particle systems with surface reactions, *Chem Eng Sci* 176:1–18, 2018.
- Manger E: *Modeling and simulation of gas solid systems in curvilinear co-ordinates*, PhD thesis, Norway, 1996, Telemark Institute of Technology.
- Matsen JM: Scale-up of fluidized bed processes: principle and practice, *Powder Technol* 88:237–244, 1996.
- Mehrabadi M, Murphy E, Subramaniam S: Development of a gas–solid drag law for clustered particles using particle-resolved direct numerical simulation, *Chem Eng Sci* 152:199–212, 2016.

- Merrow EW: Linking R&D to problems experienced in solids processing, *CEP* 81:14–22, 1985.
- Mittal R, Iaccarino G: Immersed boundary methods, *Annu Rev Fluid Mech* 37:239–261, 2005.
- Nieuwland JJ, van Sint Annaland M, Kuipers JAM, Swaaij v: Hydrodynamic modeling of riser reactors, *AIChE J* 42(6):1569–1582, 1996.
- Patankar SV, Spalding DB: A calculation procedure for heat, mass and momentum transfer in three-dimensional parabolic flows, *Int J Heat Mass Transf* 15:1787–1806, 1972.
- Peskin CS: The immersed boundary method, *Acta Numerica*: 479–517, 2002.
- Pita JA, Sundaresan S: Developing flow of a gas–particle mixture in a vertical riser, *AIChE J* 39(4):541–552, 1991.
- Tang Y, Peters EAJF, Kuipers JAM: A new drag correlation from fully resolved simulations of flow past monodisperse static arrays of spheres, *AIChE J* 61(2):688–698, 2015.
- Tang Y, Buck B, Heinrich S, Deen NG, Kuipers JAM: Interface-resolved simulations of normal collisions of spheres on a wet surface, *AIChE Journal* 63(11):4774–4787, 2017.
- Van der Hoef MA, van Sint Annaland M, Kuipers JAM: Computational fluid dynamics for dense gas–solid fluidized beds: a multi-scale modeling strategy, *Chem Eng Sci* 59:5157–5165, 2004.
- Van der Hoef MA, van Sint Annaland M, Deen NG, Kuipers JAM: Numerical simulation of dense gas–solid fluidized beds: a multi-scale modeling strategy, *Annu Rev Fluid Mech* 40:47–70, 2008.
- Van Sint Annaland M, Bokkers GA, Goldschmidt MJV, Olaofe OO, van der Hoef MA, Kuipers JAM: Development of a multi-fluid model for poly-disperse dense gas–solid fluidized beds, part I: model derivation and numerical implementation, *Chem Eng Sci* 64:4222–4236, 2009a.
- Van Sint Annaland M, Bokkers GA, Goldschmidt MJV, Olaofe OO, van der Hoef MA, Kuipers JAM: Development of a multi-fluid model for poly-disperse dense gas solid fluidized beds, part II: segregation in binary particle mixtures, *Chem Eng Sci* 64:4237–4246, 2009b.
- Verma V, Deen NG, Padding JT, Kuipers JAM: Two-fluid modelling of three-dimensional cylindrical gas–solid fluidized beds using the kinetic theory of granular flow, *Chem Eng Sci* 102:227–245, 2013.
- Verma V, Padding JT, Deen NG, Kuipers JAM: Numerical investigation on the effect of pressure on fluidization in a 3D fluidized bed, *Ind Eng Chem Res* 53:17487–17498, 2014a.
- Verma V, Padding JT, Deen NG, et al: Bubble dynamics in a 3D gas–solid fluidized bed using ultrafast electron beam X-ray tomography and two-fluid model, *AIChE J* 60(5): 1632–1644, 2014b.
- Verma V, Padding JT, Deen NG, Kuipers JAM: Effect of bed size on hydrodynamics in 3D gas–solid fluidized beds, *AIChE J* 61(5):1492–1506, 2015.
- Wen CY, Yu YH: A generalized method for predicting the minimum fluidization velocity, *AIChE J* 12(3):610–612, 1966.
- Werther J: Bubble growth in large diameter fluidized beds, international fluidization conference, Pacific Grove, USA, 1975. In Kearns DL, editor: *Fluidization technology*, Washington, DC, 1976, Hemisphere Publishing Co., pp 215–235.
- Yang L, Padding JT, Kuipers JAM: Modification of kinetic theory of granular flow for frictional spheres, part I: two-fluid model derivation and numerical implementation, *Chem Eng Sci* 152:767–782, 2016a.
- Yang L, Padding JT, Kuipers JAM: Modification of kinetic theory of granular flow for frictional spheres, part II: model validation, *Chem Eng Sci* 152:783–794, 2016b.
- Yang L, Padding JT, Buist KA, Kuipers JAM: Three-dimensional fluidized beds with rough spheres: validation of a two fluid model by magnetic particle tracking and discrete particle simulations, *Chem Eng Sci* 174:238–258, 2017a.
- Yang L, Padding JT, Kuipers JAM: Partial slip boundary conditions for collisional granular flows at flat frictional walls, *AIChE J* 63(6):1853–1871, 2017b.